Energy Harvesting from Random Vibrations of Piezoelectric Cantilevers and Stacks

A Thesis
Presented to
The Academic Faculty

By

Sihong Zhao

In Partial Fulfillment
of the Requirements for the Degree
Master of Science in Mechanical Engineering

Georgia Institute of Technology
August, 2013

Energy Harvesting from Random Vibrations of Piezoelectric Cantilevers and Stacks

Approved by:

Dr. AlperErturk
School of Mechanical Engineering
Georgia Institute of Technology

Dr. Aldo Ferri
School of Mechanical Engineering
Georgia Institute of Technology

Dr. Laurence Jacobs
College of Engineering
Georgia Institute of Technology

Date Approved: October 19th, 2012

ACKNOWLEDGEMENTS

I would like to offer my sincerest gratitude to my graduate advisor, Dr. Alper Erturk, for offering me the opportunity to conduct research in Smart Structures and Dynamical Systems Laboratory at Georgia Tech in April 2011. During my graduate study, Dr. Erturk not only gave me detailed guidance and innovative inputs to my research project, but also paid a great deal of patience in teaching the fundamentals to me as well as helping me with experimental setup and trouble shooting. I am very thankful to have him as my graduate advisor.

I would like to thank Dr. Aldo Ferri and Dr. Larry Jacobs who serve on my reading committee and gave valuable feedback to me. I took dynamic and vibration courses from Dr. Ferri and wave propagation course from Dr. Jacobs. I learned a lot from their courses and was also inspired by their passion for teaching and researching.

I also want to thank my lab mates: Lejun Cen, Martin Cacan, and Algan Samur. We helped and support each other. I enjoyed the atmosphere in my lab and appreciate this friendship.

My advisor and professors from undergraduate school, Miami University of Ohio, continue giving me suggestions on my research and career path, after my graduation from there. I am deeply moved and want to take this opportunity to thank them too.

I want to thank my friends and family, who always concern with my personal growth, and encourage me to pursue my career and dreams. Especially I want to say thank you to my mother, who has showed generous love to me. She with her wisdom can always guide me and take away my pressure.

At last, support from the U.S. Department of Commerce, National Institute of Standards and Technology, Technology Innovation Program, Cooperative Agreement Number 70NANB9H9007,

“Self-Powered Wireless Sensor Network for Structural Health Prognosis,” is gratefully acknowledged.

TABLE OF CONTENTS

ACKNOWLEDGEMENTS III

LIST OF TABLES IX

LIST OF FIGURES X

SUMMARY XV

CHAPTER 1

INTRODUCTION 1

1.1 Motivation 1

1.2 Research objective 3

1.3 Outline of thesis 4

CHAPTER 2

BACKGROUND AND SIGNIFICANCE 5

2.1 Existing modeling efforts of energy harvesting from random vibrations 5

2.2 Significance of the current research 9

CHAPTER 3

BROADBAND RANDOM EXCITATION OF A CANTILEVERED BIMORPH 10

3.1 Distributed-parameter electroelastic modeling 10

3.2 Steady-state response to harmonic excitation and electroelastic FRFs 13

3.3 Broadband random excitation: analytical solution.....17

3.4 Broadband random excitation: numerical solutions.....21

3.4.1 Fourier series-based Runge-Kutta solution 21

3.4.2 Euler-Maruyama solution 24

3.5 Experimental validation.....25

3.5.1 Experimental setup and cantilevered bimorph 25

3.5.2 Experimental validation of electroelastic FRFs 29

3.5.3 Broadband random excitation 31

3.5.4 Expected value of the electrical power output.....34

3.5.5 Mean-square value of the shunted vibration response.....37

3.6 Comparison of various piezoelectric materials 40

3.6.1 Electroelastic FRFs.....42

3.6.2 Expected value of the electrical power output.....46

3.6.3 Mean-square value of the vibration response.....47

3.7 Conclusions.....48

CHAPTER 4

BROADBAND RANDOM EXCITATION OF A MULTILAYER STACK 50

4.1 Electroelastic modeling.....50

4.2 Broadband random excitation: analytical solution ….....52

4.3 Broadband random excitation: numerical solutions 53

4.3.1 Fourier series-based Runge-Kutta solution.....53

4.3.2 Euler-Maruyama solution.....54

4.4 Experimental validation ….....55

4.4.1 Experimental setup and multilayer stack.....55

4.4.2 Experimental validation of electroelastic FRFs.....56

4.4.3 Harmonic excitation.....57

4.4.4 Broadband random excitation.....59

4.5 Comparison of various piezoelectric materials.....62

4.5.1 Electroelastic FRFs.....63

4.5.2 Expected value of the electrical power output.....64

4.6 Conclusions 66

CHAPTER 5

BAND-LIMITED RANDOM EXCITATION OF THE CANTILEVER AND STACK CONFIGURATIONS.....67

5.1 Cantilevered bimorph.....67

5.1.1 Random excitation with 0-200 Hz bandwidth.....68

5.1.2 Random excitation with 0-1 kHz bandwidth.....69

5.1.3 Random excitation with 0-5 kHz bandwidth.....71

5.2 Multilayer piezostack 72

5.2.1 Random excitation with 0-10 Hz bandwidth.....73

5.2.2 Random excitation with 0-50 Hz bandwidth.....74

5.2.3 Random excitation with 0-140 Hz bandwidth.....75

5.3 Conclusions 76

CHAPTER 6

CONCLUSIONS AND RECOMMENDATIONS FOR FUTURE WORK 78

6.1 Conclusions.....78

6.2 Recommendations for future work.....80

REFERENCES.....81

LIST OF TABLES

Table 1. Modal electromechanical coupling and equivalent capacitance terms..... 14

Table 2. Geometric and material properties of the PZT-5H cantilevered bimorph used in experiments ....……..28

Table 3. Elastic, piezoelectric, and dielectric properties of the materials ……..…41

Table 4. Mechanical damping ratio for the fundamental vibration mode of each bimorph cantilever …….....…….....42

Table 5. Geometric and material properties of the PZT-5H stack used in experiments ……...56

Table 6. Piezoelectric, and dielectric properties of the materials ....……..62

Table 7. Comparison of volumetric stack requirement for different piezoelectric materials to generate 1 mW mean power output under 1 MPa RMS pressure .....…...65

LIST OF FIGURES

Figure 1. A three-span multi-girder steel bridge in Roanoke, VA, the accelerometer attached on the bridge, and measured acceleration 5

Figure 2. Bimorph piezoelectric energy harvester configurations under base excitation.....11

Figure 3. Details of the experimental setup of energy harvesting using cantilever bimorph....…27

Figure 4. Close-up view and side view of the brass-reinforced cantilevered bimorph…..…...28

Figure 5. Experimental validation of the electroelastic FRFs of cantilevered bimorph…..…30

Figure 6. Analytically obtained voltage and tip velocity FRFs of the PZT-5H bimorph ……31

Figure 7. A sample of time history of the measured random base acceleration and its PSD for a broad frequency range ……..…….……..32

Figure 8. PSD of base acceleration shown in Fig. 7 extracted directly from the data acquisition system, estimated using the Welch method, and averaged based on the Welch estimate …….……...…….33

Figure 9. PSD values estimated from the Welch algorithm for all tests at three base excitation levels ……...…….…...….....34

Figure 10. Comparison of the analytical and numerical simulations of mean power output with the experimental measurements for a set of resistive loads.....35

Figure 11. Comparison of the analytical and numerical simulations of mean power output with the experimental measurements for a set of resistive loads at different PSD levels of base acceleration ..……..……..…….…..…36

Figure 12. Comparison of the experimental results and a hybrid analytical solution of mean power output for a set of resistive loads at different PSD levels of base acceleration ……...……..…..…..37

Figure 13. Comparison of the analytical and numerical simulations of mean-square shunted tip velocity with the experimental measurements for a set of resistive loads …...…….....38

Figure 14. Comparison of the analytical and numerical simulations of mean-square shunted tip velocity with the experimental measurements for a set of resistive loads at different PSD levels of base acceleration ……..……...38

Figure 15. Comparison of the experimental results and a hybrid analytical solution of mean-square shunted tip velocity for a set of resistive loads at different PSD levels of base acceleration ……..……..39

Figure 16. Maximum expected power output and minimum mean-square shunted tip velocity at different levels of base acceleration PSD …….....….40

Figure 17. Voltage – to – base acceleration FRFs and tip velocity – to – base acceleration FRFs of the PZT-5H bimorph for a set of resistors …..…….....…...43

Figure 18. Voltage – to – base acceleration FRFs and tip velocity – to – base acceleration FRFs of the PZT-8 bimorph for a set of resistors..... .……...…….44

Figure 19. Voltage – to – base acceleration FRFs and tip velocity – to – base acceleration FRFs of the PMN-PZT bimorph for a set of resistors ..……..……..……...……45

Figure 20. Voltage – to – base acceleration FRFs and tip velocity – to – base acceleration FRFs of the PMN-PZT-Mn bimorph for a set of resistors .……...…..46

Figure 21. Expected power output for bimorphs made of different piezoelectric materials ...….47

Figure 22. Mean square value of tip velocity for bimorphs made of different piezoelectric materials.....47

Figure 23. Schematic of a multilayer piezostack used for energy harvesting under random excitation 50

Figure 24. Experimental setup of energy harvesting using piezostack 55

Figure 25. Voltage – to – pressure FRFs of the PZT-5H stack for a set of resistors 57

Figure 26. Peak value of power output (normalized with respect to the stack volume) under harmonic excitation at 20 Hz and different pressure levels.....58

Figure 27. Peak value of power output (normalized with respect to the stack volume and input pressure) under harmonic excitation at 20 Hz.....58

Figure 28. Maximum power output (normalized with respect to the stack volume and input pressure) under harmonic excitation at 10 Hz, 20 Hz and 30 Hz 59

Figure 29. An example of time history of the pressure applied on the stack.....60

Figure 30. PSD of the pressure signal in Fig. 29.....60

Figure 31. Comparison of experimental results, numerical simulations, and analytical predictions of power generation (normalized with respect to the stack volume and input pressure) at a pressure level 58 kPa 61

Figure 32. Experimental results and analytical predictions of maximum power generation at different pressure levels 61

Figure 33. Voltage – to – force FRFs of the PZT-5H stack for a set of resistors 63

Figure 34. Voltage – to – force FRFs of the PZT-8 stack for a set of resistors 63

Figure 35. Voltage – to – force FRFs of the PMN-PZT stack for a set of resistors 63

Figure 36. Voltage – to – force FRFs of the PMN-PZT-Mn stack for a set of resistors 64

Figure 37. Voltage – to – force FRFs of the PZT-5A stack for a set of resistors.....……..64

Figure 38. Expected power output (normalized with respect to the stack volume and input pressure) for stacks made of different piezoelectric materials.…….…….....…...65

Figure 39. Voltage – to – base acceleration FRFs and (b) tip velocity – to – base acceleration FRFs of the PZT-5H bimorph cantilever for a set of resistors …….…..…67

Figure 40. PSD of a 0-200 Hz random base acceleration signal …….....68

Figure 41. Comparison of analytical predictions, numerical simulations, and experimental results of expected power generation of cantilever under 0-200 Hz random excitation.....69

Figure 42. Comparison of analytical predictions, numerical simulations, and experimental results of mean-square tip velocity of cantilever under 0-200 Hz random excitation …...…..69

Figure 43. PSD of a 0-1k Hz random base acceleration signal …….....70

Figure 44. Comparison of analytical predictions, numerical simulations, and experimental results of expected power generation of cantilever under 0-1 kHz random excitation …...…..70

Figure 45. Comparison of analytical predictions, numerical simulations, and experimental results of mean-square tip velocity of cantilever under 0-1 kHz random excitation….....71

Figure 46. PSD of a 0-5 kHz random base acceleration signal …….....71

Figure 47. Comparison of experimental results, numerical simulations, and analytical predictions of mean-square of tip velocity ……...72

Figure 48. Comparison of analytical predictions, numerical simulations, and experimental results of mean-square of tip velocity of cantilever under 0-5kHz random excitation...….....72

Figure 49. Voltage – to – force FRFs of the PZT-5H stack for a set of resistors …..…….....73

Figure 50. PSD of a 0-10 Hz random excitation signal …….....74

Figure 51. Comparison of analytical predictions, numerical simulations, and experimental results of expected power generation of piezostack (0-10 Hz random excitation) …….....74
Figure 52. PSD of a 0-50 Hz random excitation signal …….....75
Figure 53. Comparison of analytical predictions, numerical simulations, and experimental results of expected power generation of piezostack (0-50 Hz random excitation) .....……..75
Figure 54. PSD of a 0-140 Hz random excitation signal …..…….....76
Figure 55. Comparison of analytical predictions, numerical simulations, and experimental results of expected power generation of piezostack (0-140Hz random excitation) .....…….....76

SUMMARY

Electromechanical modeling efforts in the research field of vibration-based energy harvesting have been mostly focused on deterministic forms of vibrational input as in the typical case of harmonic excitation at resonance. However, ambient vibrational energy often has broader frequency content than a single harmonic, and in many cases it is entirely stochastic. As compared to the literature of harvesting deterministic forms of vibrational energy, few authors presented modeling approaches for energy harvesting from broadband random vibrations. These efforts have combined the input statistical information with the single-degree-of-freedom (SDOF) dynamics of the energy harvester to express the electromechanical response characteristics. In most cases, the vibrational input is assumed to have broadband frequency content, such as white noise. White noise has a flat power spectral density (PSD) that might in fact excite higher vibration modes of an electroelastic energy harvester. In particular, cantilevered piezoelectric energy harvesters constitute such continuous electroelastic systems with more than one vibration mode.

The main component of this thesis presents analytical and numerical electroelastic modeling, simulations, and experimental validations of piezoelectric energy harvesting from broadband random excitation. The modeling approach employed herein is based on distributed-parameter electroelastic formulation to ensure that the effects of higher vibration modes are included. The goal is to predict the expected value of the power output and the mean-square shunted vibration response in terms of the given PSD or time history of the random vibrational input. The analytical method is based on the PSD of random base excitation and distributed-parameter frequency response functions of the coupled voltage output and shunted vibration response. The first one of the two numerical solution methods employs the Fourier series

representation of the base acceleration history in a Runge-Kutta-based ordinary differential equation solver while the second method uses an Euler-Maruyama scheme to directly solve the resulting electroelastic stochastic differential equations. The analytical and numerical simulations are compared with several experiments for a brass-reinforced PZT-5H cantilever bimorph under different random excitation levels. In addition to base-excited cantilevered configurations, energy harvesting using prismatic piezoelectric stack configurations is investigated. Electromechanical modeling and numerical simulations are given and validated through experiments for a multi-layer PZT-5H stack. After validating the electromechanical models for specific experimentally configurations and samples, various piezoelectric materials are compared theoretically for energy harvesting from random vibrations. Finally, energy harvesting from narrowband random vibrations using both configurations are investigated theoretically and experimentally.

CHAPTER 1

INTRODUCTION

1.1 Motivation

Vibration-based energy harvesting for low-power electricity generation has been heavily researched over the last decade [1-5]. The motivation in this research field is due to the reduced power requirement of small electronic components, such as the wireless sensor networks used in passive and active monitoring applications. The ultimate goal is to enable autonomous wireless electronic systems by recovering the waste vibrational energy available in their environment so that maintenance requirement for battery replacement and chemical waste of conventional batteries can be minimized. Among the basic transduction mechanisms that can be used for vibration-to-electricity conversion (electromagnetic, electrostatic, piezoelectric, and magnetostrictive conversion methods as well as the use of electroactive polymers [6-16]), piezoelectric transduction has received the greatest attention due to the high power density and ease of application of piezoelectric materials [4].

The existing electromechanical modeling efforts of vibration-based energy harvesting using piezoelectric and other transduction mechanisms have mostly focused on harmonic excitation at resonance. A variety of electromechanical models and energy harvester configurations have been investigated for energy harvesting under harmonic excitation. Closed-form solutions for power generation and vibration response of harvesters are generally available in the literature. However, ambient vibrational energy often has broader frequency content than a single harmonic and in many cases it is entirely stochastic. As compared to harmonic vibration,

random vibration processes involve more complicated frequency information and statistical properties.

Among the limited studies on piezoelectric energy harvesting from random vibration, many are pure experimental studies or pure numerical simulations. Very few authors presented modeling approaches and most of them use single-degree-of-freedom (SDOF) energy harvester models. As an alternative to SDOF modeling and analysis efforts, in this thesis, a distributed-parameter electroelastic model is employed. The motivation for distributed-parameter modeling emerges from the fact that broadband random vibrations may in fact excite higher vibration modes of an electroelastic energy harvester, which can be significant for a configuration with lightly damped higher modes. Based on the distributed-parameter electroelastic model, analytical solutions of the expected electrical power output as well as shunted vibration response of the harvester are obtained. In addition, two numerical solutions are developed and experiments are performed to validate the solutions.

In the literature of energy harvesting from random vibrations, most authors assume broadband random vibration (such as ideal white noise) as the energy source. Therefore, this thesis starts with the assumption of broadband random excitation as vibrational input, and then considers band-limited random vibrational input, with the motivation to develop analytical and numerical solutions to predict the coupled responses of the system.

The two energy harvester configurations investigated in this thesis are cantilevered bimorph and multilayer stack, which are two most popular piezoelectric energy harvester configurations.

1.2 Research Objectives

The objective of this research is to theoretically and experimentally investigate piezoelectric energy harvesting from random vibrations of based-excited bimorph cantilevers and axially loaded multilayer stacks. To this end, the goals in this thesis can be summarized as follows:

- Development of both multi-mode and single-mode frequency-domain analytical and time-domain numerical solutions for the expected electrical power output and mean-square shunted vibration response of cantilevered energy harvesters in response to random base excitation
- Development of analytical and numerical solutions to predict the expected power in response to random axial loading of multilayer piezoelectric stacks
- Investigation of the effects of higher vibration modes on the expected power output and shunted vibration response in the cantilever case
- Experimental validation of the analytical and numerical solutions through experiments at various excitation levels
- Experimental validation of the solutions for both broadband and band-limited random excitations
- Comparison of various piezoelectric materials in terms of their energy harvesting performance under broadband random excitation

1.3 Outline of Thesis

In Chapter 2, the background and literature review of electromechanical modeling efforts of energy harvesting from broadband random excitation are provided, and the significance of this research is discussed. After that Chapters 3 and 4 present piezoelectric energy harvesting from broadband random vibration using cantilevered bimorph and multiplayer stack, respectively. In each of these two chapters, electroelastic models are summarized, analytical solutions, two numerical methods, and experimental validations are discussed. Comparisons of various piezoelectric materials in terms of their random power generation performance are also provided at the end of both chapters. Chapter 5 provides the validations of the analytical and numerical solutions under band-limited random vibration for cantilevered bimorphs and multilayer stacks. Finally, the last chapter discusses the conclusions and provides recommendations for future work in this field.

CHAPTER 2

BACKGROUND AND SIGNIFICANCE

2.1 Existing modeling efforts of energy harvesting from random vibrations

Most of the existing electromechanical modeling efforts on vibration-based energy harvesting have been based on the assumption that the vibrational input is deterministic, as in the typical case of harmonic excitation of linear and nonlinear energy harvesters at or around resonance [6-16]. Closed-form expressions of for generation and optimality conditions have been well developed by several authors for deterministic forms of excitation [17-20]. These efforts contribute to the design and performance evaluation of linear and nonlinear energy harvesters under harmonic excitation.

Harmonic excitation is a simple and rather idealized representation of real-world ambient vibrations. In many cases, ambient vibrational energy is non-harmonic or entirely stochastic with broad frequency content (Fig. 1). As compared to the literature of harvesting deterministic forms of energy, rather few research groups have investigated energy harvesting from random vibrations and employed different electromechanical models. Typically, the excitation source is assumed to be ideal white noise, which is a broadband random signal that has a flat power spectral density (PSD) in frequency domain.

(a) (b)

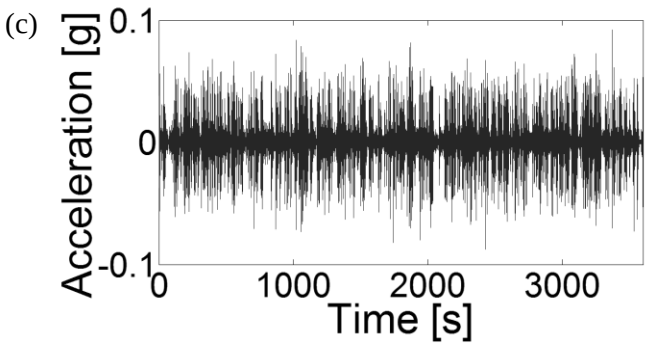

Figure 1 (a) A three-span multi-girder steel bridge in Roanoke, VA; (b) the accelerometer attached on the bridge; (c) measured acceleration (from NIST report [40])

Single-degree-of-freedom (SDOF) modeling is the most commonly used approach in the theoretical exploration of energy harvesters driven by broadband random excitation. Halvorsen [21] derived closed-form expressions for the power output, optimal load, and proof mass displacement based on linear SDOF modeling, and verified the resulting expressions by solving the Fokker-Planck equation. The results were also compared with those obtained from the same model under harmonic excitation and differences were reported. Adhikari et al. [22] also used a linear SDOF model to describe the stochastic dynamics for the fundamental vibration mode of an energy harvester. Analytical expressions of the harvested power and optimal load were derived, and illustrated using numerical examples. Scruggs [23] investigated the optimal control of a linear energy harvester network for increased power flow to a storage system under random excitation.

Daqaq [24] considered hardening stiffness in the SDOF formulation for electromagnetic energy harvesting and concluded that the monostable Duffing oscillator did not provide an enhancement over the typical linear oscillators under Gaussian white and colored random excitations and contemporaneous experiments by Barton et al. [25] for electromagnetic energy

harvesting provided consistent results. Based on SDOF modeling, Cottone et al. [26] and Gammaitoni et al. [26] suggested that carefully designed nonlinear oscillators could potentially outperform the linear ones under noise excitation for both bistable and monostable configurations.

Ferrari et al. [27] numerically studied a bistable SDOF energy harvesting system under broadband random excitation by using the Euler-Maruyama method. Litak et al. [28] numerically simulated a bistable piezomagnetoelastic energy harvester (introduced by Erturk et al. [29]) under Gaussian white noise and observed a positive correlation between standard deviations of the random excitation and of the voltage output. In particular, they [28] focused on the potential of exploiting "stochastic resonance" in energy harvesting, as formerly discussed by McInnes et al. [30] through another SDOF representation. Ali et al. [31] developed a linearized SDOF model for broadband random excitation of bistable piezomagnetoelastic energy harvesters. They showed that there existed a cut-off standard deviation of the input excitation below which the power output was very low. Daqaq [32] gave a theoretical study on the response of an inductive SDOF bistable energy harvester to white and exponentially correlated Gaussian noise. For Gaussian white noise excitation, the exact probability distribution function was expressed in order to obtain a closed-form expression of mean power output.

Nguyen et al. [33] studied a wideband MEMS electrostatic energy harvester using a lumped-parameter model. They experimentally compared the PSD of voltage output for different levels of broadband random inputs. They also examined the relationship between the output power and PSD of excitation in addition to providing finite-element simulations. Some research groups also utilized SPICE, a numerical circuit simulator, to simulate the harvested energy in response to random vibrations [34-36]. Tvedt et al. [37] also considered broadband vibration

excitation when they investigated the nonlinear behavior of an electrostatic energy harvester along with the effect of bias voltage.

As another common piezoelectric configuration, piezostack has been employed in many harvester designs. Stack-based energy harvesters have been mostly investigated under deterministic excitation in the existing literature. The applied mechanical load on the harvesters are often considered to be harmonic as in the following examples. Goldfarb et al. [46] analyzed a piezoelectric stack under harmonic mechanical load using a lumped parameter model and derived the expression of power efficiency. The results were validated experimentally by performing frequency and resistance sweeps. Maximum power generation was claimed to occur at low frequency which was several orders of magnitude below the resonance frequency of the stack. The power efficiency also had a weaker dependence on resistance than frequency. Feenstra et al. [47] designed an energy harvester that employed a mechanically amplified piezoelectric stack and converted the dynamic tension in the backpack strap to electrical energy. It was reported that a mean power of approximately 0.4mW was generated for a 220N load. As an alternative of a conventional flex-tensional piezoelectric transducer, which might result cracks in piezoelectric element, Li et al. [48] designed a flex-compressive mode transducer that used two piezoelectric stacks and two bow-shaped elastic plates. They derived the expression of power generation under resonance driving conditions and reported that a maximum power of 14.6mW was harvested under a 1g peal-to-peak excitation at the transducer's resonance frequency.

2.2 Significance of the current research

As compared to the literature of energy harvesting from deterministic vibrational source, typically harmonic at resonance, very few authors have investigated random vibrations and most of them employed SDOF models. Since broadband random excitation might excite lightly-damped higher vibration modes of the harvester, in this research, a distributed-parameter electroelastic model is used. The expected power output and mean-square shunted vibration response are expressed in terms of the excitation PSD and the electroelastic frequency response functions (FRFs) in the analytical solution. After that, the numerical electroelastic solutions are presented based on two separate approaches. The deterministic approach represents the excitation history in terms of its Fourier series expansion to use in the first-order electroelastic equations for a Runge-Kutta scheme while the stochastic approach directly employs an Euler-Maruyama scheme to solve the resulting first-order stochastic differential equations. Experimental results are then presented to validate analytical and numerical predictions. Electrical power generation and its shunt damping effect at different random vibration levels are investigated.

The analytical solutions and numerical simulations are proved to be effective tools to predict the power generation and shunted vibration response of the harvesters under both broadband and band-limited random vibrations. Although computationally slower than the analytical solutions, the two numerical simulations are also shown to be useful tools when handling stochastic input. With these established mathematical tools, different piezoelectric materials can be compared and optimized in terms of their energy harvesting performance under random excitation.

CHAPTER 3

BROADBAND RANDOM EXCITATION OF A CANTILEVERED BIMORPH

3.1 Distributed-parameter electroelastic modeling

Figure 2 shows symmetric bimorph piezoelectric energy harvester configurations excited by base motion in the form of translational displacement, $g(t)$, with superimposed small rotational displacement, $h(t)$. The wires originating from negligibly thin and perfectly conductive electrode pairs covering the surfaces of the piezoceramic layers are connected to a resistive electrical load (R_l). The distributed-parameter electroelastic formulation summarized in this section is based on the Euler-Bernoulli beam assumptions [11, 38]. Therefore, the energy harvesters considered herein are assumed to be thin structures so that the shear distortion and rotary inertia effects are negligible (we note that Refs. [38, 39] present modeling of piezoelectric energy harvesters with moderate thickness). As a consequence, the tensorial form of the linear piezoelectric constitutive equations can be given in the plane-stress form as

$$\begin{Bmatrix} T_1 \\ D_3 \end{Bmatrix} = \begin{bmatrix} \bar{c}_{11}^{E} & -\bar{e}_{31} \\ \bar{e}_{31} & \bar{\varepsilon}_{33}^{S} \end{bmatrix} \begin{Bmatrix} S_1 \\ E_3 \end{Bmatrix} \tag{1}$$

where T_1 is the stress component, D_3 is the electric displacement component, S_1 is the strain component, E_3 is the electric field component, 3-direction is the poling direction (z-direction in Fig. 1), and 1-direction is the axial direction (x-direction in Fig. 1). In addition, $\bar{e}_{31}$ is the effective piezoelectric stress constant, $\bar{c}_{11}^{E}$ is elastic stiffness component (Young's modulus) at constant electric filed, and $\bar{\varepsilon}_{33}^{S}$ is the permittivity component at constant strain and an over-bar

denotes that the respective parameter is reduced for the plane-stress conditions. Thus, for a beam-like thin cantilever, the plane-stress elastic, piezoelectric and dielectric parameters can be given in terms of the 3-D electroelasticity components as

$$\bar{c}_{11}^{E} = 1/s_{11}^{E},\ \bar{e}_{31} = d_{31}/s_{11}^{E},\ \bar{\varepsilon}_{33}^{S} = \varepsilon_{33}^{T} - d_{31}^{2}/s_{11}^{E} \tag{2}$$

where s_{11}^{E} is the elastic compliance at constant electric field, d_{31} is the commonly referred piezoelectric strain constant, and ε_{33}^{T} is the permittivity component at constant stress. Note that the substructure material is typically an isotropic metal.

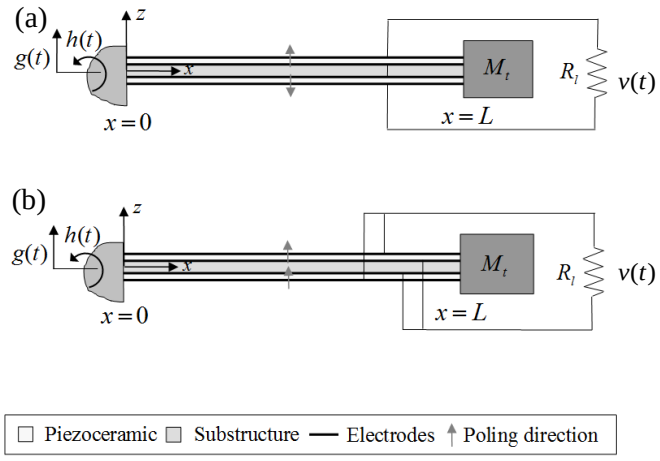

Figure 2. Bimorph piezoelectric energy harvester configurations under base excitation: (a) series and (b) parallel connection of the piezoelectric layers.

The governing linear electroelastic equations of a bimorph piezoelectric energy harvester (Fig. 1) in the physical coordinates are [11, 38]

$$D\frac{\partial^4 w_{rel}(x,t)}{\partial x^4} + c_s\frac{\partial^5 w_{rel}(x,t)}{\partial x^4 \partial t} + c_m\frac{\partial w_{rel}(x,t)}{\partial t} + m\frac{\partial^2 w_{rel}(x,t)}{\partial t^2} - \vartheta v(t)\left[\frac{d\delta(x)}{dx} - \frac{d\delta(x-L)}{dx}\right] = -\left[m + M_t\delta(x-L)\right]\frac{\partial^2 w_b(x,t)}{\partial t^2} \tag{3}$$

$$C_p^{eq}\frac{dv(t)}{dt}+\frac{v(t)}{R_l}+\vartheta\int_0^L\frac{\partial^3 w_{rel}(x,t)}{\partial x^2\partial t}dx=0 \tag{4}$$

where $w_b(x,t)=g(t)+xh(t)$ is the effective base displacement as the excitation input, $w_{rel}(x,t)$ is the vibration response (transverse displacement of the neutral axis relative to the moving base at position x and time t), $v(t)$ is the voltage response across the external resistive load, D is the bending stiffness of the beam, m is the mass per unit length of the beam, c_m is the external damping coefficient (mass-proportional damping), c_s is the internal damping coefficient of the composite structure (stiffness-proportional damping), M_t is the tip mass, C_p^{eq} is the equivalent capacitance of the piezoceramic layers, ϑ is the electromechanical coupling term in the physical coordinates, and $\delta(x)$ is the Dirac delta function. The electromechanical coupling term is $\vartheta=\overline{e}_{31}b(h_p+h_s)/2$ if the piezoelectric layers are connected in series and $\vartheta=\overline{e}_{31}b(h_p+h_s)$ if the piezoelectric layers are connected in parallel (where b is the width of the layers, h_p is the thickness of each piezoceramic layer, and h_s is the thickness of the substructure layer). Likewise the equivalent capacitance is $C_p^{eq}=\overline{\varepsilon}_{33}^S bL/2h_p$ for series connection and $C_p^{eq}=2\overline{\varepsilon}_{33}^S bL/h_p$ for parallel connection (where L is the overhang length).

If the vibration response (relative to its moving base) in the physical coordinates is expressed in terms of the mass-normalized eigenfunctions (mode shapes), $\phi_r(x)$, and the modal coordinates, $\eta_r(t)$, for the rth mode such that

$$w_{rel}(x,t)=\sum_{r=1}^{\infty}\phi_r(x)\eta_r(t) \tag{5}$$

where the eigenfunctions are obtained from the undamped and electromechanically uncoupled problem [11, 38], then, following the analytical modal analysis procedure [40], the electromechanically coupled ordinary differential equations in the modal coordinates are obtained as

$$\ddot{\eta}_r(t) + 2\zeta_r \omega_r \dot{\eta}_r(t) + \omega_r{}^2 \eta_r(t) - \tilde{\theta}_r v(t) = f_r(t) \tag{6}$$

$$C_p^{eq} \dot{v}(t) + \frac{v(t)}{R_l} + \sum_{r=1}^{\infty} \tilde{\theta}_r \dot{\eta}_r(t) = 0 \tag{7}$$

Here, an over-dot $(\dot{})$ represents differentiation with respect to time, ζ_r is the modal mechanical damping ratio, ω_r is the undamped natural frequency (close to the short-circuit resonance frequency, ω_r^{sc} , for the light mechanical damping condition: $\zeta_r \ll 1$), $\tilde{\theta}_r$ is the modal electromechanical coupling term, and $f_r(t)$ is the modal mechanical forcing function which depends on the forms of $g(t)$ and $h(t)$.

3.2 Steady-state response to harmonic excitation and electroelastic FRFs

If the motion of the vibrating base in Fig. 1 is harmonic of the form $g(t) = W_0 e^{j\omega t}$ and $h(t) = \theta_0 e^{j\omega t}$ (where W_0 and θ_0 are the translational and small rotational displacement amplitudes of the base, respectively, ω is the excitation frequency, and j is the unit imaginary number), hence $f_r(t) = F_r e^{j\omega t}$, the steady-state voltage response ($v(t) = V e^{j\omega t}$ where V is the complex voltage) of the cantilevers shown in Fig. 1 can be given as [11, 38]

$$v(t) = Ve^{j\omega t} = \frac{\sum_{r=1}^{\infty} \frac{-j\omega\tilde{\theta}_r F_r e^{j\omega t}}{\omega_r{}^2 - \omega^2 + j2\zeta_r\omega_r\omega}}{\frac{1}{R_l} + j\omega C_p^{eq} + \sum_{r=1}^{\infty} \frac{j\omega\tilde{\theta}_r^2}{\omega_r{}^2 - \omega^2 + j2\zeta_r\omega_r\omega}} \tag{8}$$

Here, the modal electromechanical coupling ($\tilde{\theta}_r$) and the equivalent inherent capacitance (C_p^{eq}) terms for the series and parallel connections of the piezoceramic layers are given in Table 1 (where $\phi_r'(x)$ is the derivative of $\phi_r(x)$ with respect to x).

Table 1. Modal electromechanical coupling and equivalent capacitance terms for the (a) series and (b) parallel connection cases.

(a) Series connection	
$\tilde{\theta}_r$	$\bar{e}_{31}(h_p + h_s)b\phi_r'(L)/2$
C_p^{eq}	$\bar{\varepsilon}_{33}^S bL/2h_p$
(b) Parallel connection	
$\tilde{\theta}_r$	$\bar{e}_{31}(h_p + h_s)b\phi_r'(L)$
C_p^{eq}	$2\bar{\varepsilon}_{33}^S bL/h_p$

In Eq. (8), the modal mechanical forcing term due to base excitation is

$$F_r = \omega^2 W_0 \left(m\int_0^L \phi_r(x)dx + M_t\phi_r(L) \right) + \omega^2\theta_0 \left(\int_0^L x\phi_r(x)dx + M_t L\phi_r(L) \right) \tag{9}$$

The electromechanically coupled vibration response of the energy harvester beam (relative to its moving base) at steady state is then

$$w_{rel}(x,t)=\sum_{r=1}^{\infty}\frac{\left[f_r(t)+\tilde{\theta}_r v(t)\right]\phi_r(x)}{\omega_r{}^2-\omega^2+j2\zeta_r\omega_r\omega}=\sum_{r=1}^{\infty}\frac{\left[F_r+\tilde{\theta}_r V\right]\phi_r(x)e^{j\omega t}}{\omega_r{}^2-\omega^2+j2\zeta_r\omega_r\omega} \tag{10}$$

which includes the effect of piezoelectric shunt damping due to the $\tilde{\theta}_r v(t)$ term, where $v(t)$ is given by Eq. (8). Using Eqs. (8) and (10), it is possible to define electroelastic FRFs.

If the base is assumed to be not rotating ($h(t)=0$), i.e. $\theta_0=0$ in Eq. (9), but translating with $g(t)=W_0e^{j\omega t}$, the modal mechanical forcing function becomes

$$F_r=-\sigma_r\omega^2W_0=\sigma_rA_0 \tag{11}$$

where A_0 is the base acceleration amplitude and σ_r is a modal forcing parameter:

$$\sigma_r=-m\int_0^L\phi_r(x)dx-M_t\phi_r(L) \tag{12}$$

One can then define the *multi-mode* voltage output – to – base acceleration FRF and the vibration response – to – base acceleration FRF as follows:

$$\alpha(\omega)=\frac{v(t)}{A_0e^{j\omega t}}=\frac{\displaystyle\sum_{r=1}^{\infty}\frac{-j\omega\tilde{\theta}_r\sigma_r}{\omega_r{}^2-\omega^2+j2\zeta_r\omega_r\omega}}{\displaystyle\frac{1}{R_l}+j\omega C_p^{eq}+\sum_{r=1}^{\infty}\frac{j\omega\tilde{\theta}_r^2}{\omega_r{}^2-\omega^2+j2\zeta_r\omega_r\omega}} \tag{13}$$

$$\beta(\omega,x)=\frac{w_{rel}(x,t)}{A_0e^{j\omega t}}=\sum_{r=1}^{\infty}\frac{\left[\sigma_r+\tilde{\theta}_r\alpha(\omega)\right]\phi_r(x)}{\omega_r{}^2-\omega^2+j2\zeta_r\omega_r\omega} \tag{14}$$

The foregoing exact analytical solutions are typically truncated (in the simulations) after taking sufficient number of modes (*M* modes) to represent the system dynamics in a given frequency range such that

$$\alpha(\omega) \cong \frac{\sum_{r=1}^{M} \frac{-j\omega\tilde{\theta}_r\sigma_r}{\omega_r{}^2 - \omega^2 + j2\zeta_r\omega_r\omega}}{\frac{1}{R_l} + j\omega C_p^{eq} + \sum_{r=1}^{M} \frac{j\omega\tilde{\theta}_r^2}{\omega_r{}^2 - \omega^2 + j2\zeta_r\omega_r\omega}} \tag{15}$$

$$\beta(\omega, x) \cong \sum_{r=1}^{M} \frac{\left[\sigma_r + \tilde{\theta}_r\alpha(\omega)\right]\phi_r(x)}{\omega_r{}^2 - \omega^2 + j2\zeta_r\omega_r\omega} \tag{16}$$

If the energy harvester beam is excited close to a natural frequency, i.e., $\omega \cong \omega_r$, the contribution of all vibration modes other than the *r*th mode can be ignored in the summation terms of Eqs. (15) and (16) as an approximation. One can then establish the *single-mode* voltage output – to – base acceleration FRF and the vibration response – to – base acceleration FRF as follows:

$$\hat{\alpha}(\omega) = \frac{-j\omega R_l\tilde{\theta}_r\sigma_r}{\left(1 + j\omega R_l C_p^{eq}\right)\left(\omega_r{}^2 - \omega^2 + j2\zeta_r\omega_r\omega\right) + j\omega R_l\tilde{\theta}_r^2} \tag{17}$$

$$\hat{\beta}(\omega, x) = \frac{\left(1 + j\omega R_l C_p^{eq}\right)\sigma_r\phi_r(x)}{\left(1 + j\omega R_l C_p^{eq}\right)\left(\omega_r{}^2 - \omega^2 + j2\zeta_r\omega_r\omega\right) + j\omega R_l\tilde{\theta}_r^2} \tag{18}$$

where a hat (^) denotes that the respective expression is reduced for a single vibration mode (mode *r*) only. It should be noted that the foregoing single-mode relations are valid for excitation frequencies in the vicinity of the respective natural frequency only ($\omega \approx \omega_r$). Typically, the fundamental vibration mode is of interest (hence $r = 1$) and the single-mode FRFs become

$$\hat{\alpha}(\omega) = \frac{-j\omega R_l\tilde{\theta}_1\sigma_1}{\left(1 + j\omega R_l C_p^{eq}\right)\left(\omega_1{}^2 - \omega^2 + j2\zeta_1\omega_1\omega\right) + j\omega R_l\tilde{\theta}_1^2} \tag{19}$$

$$\hat{\beta}(\omega, x) = \frac{\left(1 + j\omega R_l C_p^{eq}\right)\sigma_1 \phi_1(x)}{\left(1 + j\omega R_l C_p^{eq}\right)\left(\omega_1^2 - \omega^2 + j2\zeta_1\omega_1\omega\right) + j\omega R_l \tilde{\theta}_1^2} \tag{20}$$

3.3 Broadband random excitation: analytical solution

We consider the base excitation to be Gaussian white noise-type random signal, which has a constant PSD of S_0. That is, the input PSD covers the entire frequency band with constant amplitude. Using this property of the excitation along with the electroelastic FRFs summarized in the previous section, the analytical solution for the expected (mean) power can be derived.

Recalling that the electrical power output is simply $v^2(t)/R_l$, the expected value of the power output is

$$E\left[P(t)\right] = \int_{-\infty}^{\infty} \frac{S_0}{R_l} \left|\alpha(\omega)\right|^2 d\omega \tag{21}$$

Therefore, the multi-mode analytical solution for the expected power output is obtained from

$$E\left[P(t)\right] = \int_{-\infty}^{\infty} \frac{S_0}{R_l} \left| \frac{\sum_{r=1}^{\infty} \frac{-j\omega\tilde{\theta}_r\sigma_r}{\omega_r^2 - \omega^2 + j2\zeta_r\omega_r\omega}}{\frac{1}{R_l} + j\omega C_p^{eq} + \sum_{r=1}^{\infty} \frac{j\omega\tilde{\theta}_r^2}{\omega_r^2 - \omega^2 + j2\zeta_r\omega_r\omega}} \right|^2 d\omega \tag{22}$$

which is the exact representation considering the entire spectrum of excitation and all vibration modes of the harvester.

For a compact and closed-form representation, the single-mode solution of the expected power (for the fundamental vibration mode) is estimated from

$$E\left[P(t)\right] \cong E\left[\hat{P}(t)\right] = \int_{-\infty}^{\infty} \frac{S_0}{R_l} \left|\hat{\alpha}(\omega)\right|^2 d\omega \tag{23}$$

Employing Eq. (19) in Eq. (23) yields

$$E\left[\hat{P}(t)\right] = \int_{-\infty}^{\infty} \frac{S_0}{R_l} \left| \frac{-j\omega R_l \tilde{\theta}_1 \sigma_1}{\left(1 + j\omega R_l C_p^{eq}\right)\left(\omega_1^2 - \omega^2 + j2\zeta_1\omega_1\omega\right) + j\omega R_l \tilde{\theta}_1^2} \right|^2 d\omega \tag{24}$$

Using the integration tables [41], Eq. (24) can be reduced to

$$E\left[\hat{P}(t)\right] = \frac{\pi S_0 R_l \tilde{\theta}_1^2 \sigma_1^2}{R_l \tilde{\theta}_1^2 + 2\zeta_1\omega_1\left[\left(1 + R_l^2 \tilde{\theta}_1^2 C_p^{eq}\right) + \left(2\zeta_1 + R_l C_p^{eq}\omega_1\right)\left(R_l C_p^{eq}\omega_1\right)\right]} \tag{25}$$

which is analogous to the SDOF derivations given by Halvorsen [12] and Adhikari et al. [13]. Equation (25) excludes all vibration modes other than the fundamental mode in calculation of the expected power. This single-mode approximation leads to a simple estimate for the optimal electrical load (R_l^*) for the maximum power output:

$$\frac{\partial}{\partial R_l}\left\{E\left[\hat{P}(t)\right]\right\}\Bigg|_{R_l = R_l^*} = 0 \rightarrow R_l^* = \frac{1}{\sqrt{(C_p^{eq})^2 \omega_1^2 + C_p^{eq}\tilde{\theta}_1^2}} \tag{26}$$

Back substitution yields the following expression for the single-mode estimate of the optimal expected power output:

$$E\left[\hat{P}(t)\right]_{R_l = R_l^*} = \frac{\pi S_0 \sigma_1^2 \tilde{\theta}_1^2 \sqrt{(C_p^{eq})^2 \omega_1^2 + C_p^{eq}\tilde{\theta}_1^2}}{4C_p^{eq}\tilde{\theta}_1^2\omega_1\zeta_1 + 4(C_p^{eq})^2\omega_1^3\zeta_1 + (\tilde{\theta}_1^2 + 4C_p^{eq}\omega_1^2\zeta_1^2)\sqrt{(C_p^{eq})^2 \omega_1^2 + C_p^{eq}\tilde{\theta}_1^2}} \tag{27}$$

Note that, when computing analytical solutions (particularly the multi-mode solution) by performing the frequency-domain integration numerically, the frequency range is set to be $[-\bar{\omega}, \bar{\omega}]$ such that

$$E\left[P(t)\right] = \int_{-\bar{\omega}}^{\bar{\omega}} \frac{S_0}{R_l} \left|\alpha(\omega)\right|^2 d\omega \tag{28}$$

where $\bar{\omega}$ is large enough to ensure the coverage of major vibration modes contributing to the power output given the input PSD.

The multi-mode solution for the mean-square value of the vibration response (in the displacement form) relative to moving base at point *x* is

$$E\left[w_{rel}^2(x,t)\right] = \int_{-\infty}^{\infty} S_0 \left|\beta(\omega, x)\right|^2 d\omega \tag{29}$$

yielding

$$E\left[w_{rel}^2(x,t)\right] = \int_{-\infty}^{\infty} S_0 \left| \sum_{r=1}^{\infty} \frac{\left[\sigma_r + \tilde{\theta}_r \alpha(\omega)\right] \phi_r(x)}{\omega_r^2 - \omega^2 + j2\zeta_r \omega_r \omega} \right|^2 d\omega \tag{30}$$

The single-mode approximation for the fundamental vibration mode is

$$E\left[w_{rel}^2(x,t)\right] \cong E\left[\hat{w}_{rel}^2(x,t)\right] = \int_{-\infty}^{\infty} S_0 \left|\hat{\beta}(\omega, x)\right|^2 d\omega \tag{31}$$

Using Eq. (20) in Eq. (31) yields

$$E\left[\hat{w}_{rel}^2(x,t)\right] = \frac{\pi S_0 \sigma_1^2 \phi_1^2(x) \left[(C_p^{eq})^2 R_l^2 \omega_1^2 + 2\zeta_1 C_p^{eq} R_l \omega_1 + 1\right]}{\omega_1^2 \left[2(C_p^{eq})^2 R_l^2 \omega_1^3 \zeta_1 + 2C_p^{eq} R_l^2 \tilde{\theta}_1^2 \omega_1 \zeta_1 + 4C_p^{eq} R_l \omega_1^2 \zeta_1^2 + R_l \tilde{\theta}_1^2 + 2\zeta_1 \omega_1\right]} \tag{32}$$

from which the optimal electrical load (R_l^{**}) of maximum shunt damping is obtained as

$$\frac{\partial}{\partial R_l}\left\{E\left[\hat{w}_{rel}^2(x,t)\right]\right\}\Bigg|_{R_l=R_l^{**}} = 0 \rightarrow R_l^{**} = \frac{1}{\omega_1 C_p^{eq}\left(1-2\zeta_1\right)} \tag{33}$$

Back substitution leads to the minimum mean-square vibration response for the electrical load of the maximum shunt damping:

$$E\left[\hat{w}_{rel}^2(x,t)\right]_{R_l=R_l^{**}} = \frac{2\pi S_0 C_p^{eq}\sigma_1^2(1-\zeta_1)\phi_1^2(x)}{\omega_1(\tilde{\theta}_1^2 - 4C_p^{eq}\omega_1{}^2\zeta_1^2 + 4C_p^{eq}\omega_1^2\zeta_1)} \tag{34}$$

In the experiments, it is common practice to measure the velocity response (rather than displacement) of the cantilever relative to the fixed reference frame (rather than moving base). Therefore, it is useful to modify the theoretical vibration response to predict the velocity measurement rather than post-processing the experimental data. The multi-mode solution for the mean-square velocity response at the free end of the bimorph is given by

$$E\left[\dot{w}^2(L,t)\right] = \int_{-\infty}^{\infty} S_0 \left|\beta^{modified}(\omega,L)\right|^2 d\omega \tag{35}$$

where $\beta^{modified}(\omega,L)$ is the *absolute* tip velocity FRF that can be obtained by modifying the *relative* tip displacement-to-base FRF, $\beta(\omega,L)$, [10,24]:

$$\beta^{modified}(\omega,L) = \frac{1}{j\omega} + j\omega\beta(\omega,L) \tag{36}$$

Due to the first term in Eq. (36), the velocity FRF tends to infinity around 0 Hz as a singularity. Therefore a small frequency range of $[-\varepsilon,\varepsilon]$ is excluded in the integration of Eq. (35) to give

$$E\left[\dot{w}^2(L,t)\right] = \int_{-\bar{\omega}}^{-\varepsilon} S_0 \left|\beta^{modified}(\omega,L)\right|^2 d\omega + \int_{\varepsilon}^{\bar{\omega}} S_0 \left|\beta^{modified}(\omega,L)\right|^2 d\omega \tag{37}$$

where $\varepsilon << \omega_1$. Physically, this is well justified in the experiments since the shaker (excitation source) does not emulate motion at zero frequency (rigid body motion) and the neighborhood of 0 Hz is indeed excluded in the excitation signal. Using Eq. (20) in Eq. (36) yields single-mode solution for the modified absolute tip velocity FRF, and substituting the latter into Eq. (37) yields single-mode solution for the mean-square tip velocity response.

3.4 Broadband random excitation: numerical solutions

3.4.1 Fourier series-based Runge-Kutta solution

The first numerical solution approach treats the given time series of the excitation in a deterministic fashion through its Fourier series representation. The excitation is then combined with the first-order equations for the numerical solution of the electroelastic response in time domain.

The electroelastic state variables for the *r*th vibration mode are extracted from Eqs. (6) and (7) as [38]

$$u_r^{(1)} = \eta_r(t),\ u_r^{(2)} = \dot{\eta}_r(t),\ u^{(3)} = v(t) \tag{38}$$

where $u_r^{(1)}$ is the modal displacement, $u_r^{(2)}$ is the modal velocity, and $u^{(3)}$ is the voltage output. Then the governing differential equations in the modal coordinates are expressed in the first-order form using $2M+1$ equations as

$$\begin{bmatrix} \dot{u}_1^{(1)} \\ \dot{u}_2^{(1)} \\ \vdots \\ \dot{u}_M^{(1)} \\ \dot{u}_1^{(2)} \\ \dot{u}_2^{(2)} \\ \vdots \\ \dot{u}_M^{(2)} \\ \dot{u}^{(3)} \end{bmatrix} = \begin{bmatrix} u_1^{(2)} \\ u_2^{(2)} \\ \vdots \\ u_M^{(2)} \\ -2\zeta_1\omega_1 u_1^{(2)} - \omega_1^2 u_1^{(1)} + \tilde{\theta}_1 u^{(3)} + \sigma_1 a(t) \\ -2\zeta_2\omega_2 u_2^{(2)} - \omega_2^2 u_2^{(1)} + \tilde{\theta}_2 u^{(3)} + \sigma_2 a(t) \\ \vdots \\ -2\zeta_M\omega_M u_M^{(2)} - \omega_M^2 u_M^{(1)} + \tilde{\theta}_M u^{(3)} + \sigma_M a(t) \\ -u^{(3)} / R_l C_p^{eq} - \tilde{\theta}_1 u_1^{(2)} / C_p^{eq} - \tilde{\theta}_2 u_2^{(2)} / C_p^{eq} - \cdots - \tilde{\theta}_M u_M^{(2)} / C_p^{eq} \end{bmatrix} \tag{39}$$

where $a(t)$ is the random base acceleration in the transverse direction ($a(t) = \ddot{g}(t)$) and the solution is truncated after M modes. Note that three initial conditions are required for the state variables (we assume zero initial conditions in the simulations).

The random base acceleration history is represented as a deterministic input by using its Fourier series representation:

$$a(t) \cong p_0 + \sum_{k=1}^{N} \left[p_k \cos\left(k \frac{2\pi t}{T} \right) + q_k \sin\left(k \frac{2\pi t}{T} \right) \right] \tag{40}$$

where T is the length of the time history of base acceleration, p_0 is its mean value, while p_k and q_k ($k = 1, 2, \ldots$ are positive integers) are the Fourier coefficients given by

$$p_0 = \frac{1}{T}\int_0^T a(t)dt\,,\ p_k = \frac{2}{T}\int_0^T a(t)\cos\left(k \frac{2\pi t}{T} \right)dt\,,\ q_k = \frac{2}{T}\int_0^T a(t)\sin\left(k \frac{2\pi t}{T} \right)dt \tag{41}$$

In the Fourier series representation, the number of terms N is half of the total data points in the base acceleration history and p_0 is negligible for time typical acceleration data of ambient vibrations (hence zero mean value is assumed hereafter: $p_0 = 0$). Note that the foregoing representation and the resulting solution are strictly valid for the time interval of $[0, T]$ only.

Equation (39) is then treated as a set of ordinary differential equations (ODEs). The computation is carried out by using an ODE solver, such as the ode45 algorithm in MATLAB that uses an explicit Runge-Kutta formulation.

The time histories of the voltage output and modal velocities are obtained from the system of electroelastic ODEs. If the acceleration history has zero mean value, it is known that the response forms also have zero mean value. Thus the expected value of power output can be computed by using

$$E\left[P(t)\right] = \frac{1}{T}\int_0^T \frac{v^2(t)}{R_l}\,dt = \frac{{\sigma_v}^2}{R_l} \tag{42}$$

where σ_v is the standard deviation of the voltage response.

Having obtained the modal coordinates, the tip velocity relative to moving base can be computed using

$$\dot{w}_{rel}(x,t) \cong \sum_{r=1}^{M} \phi_r(x)\dot{\eta}_r(t) = \phi_1(x)\dot{\eta}_1(t) + \phi_2(x)\dot{\eta}_2(t) + \cdots + \phi_M(x)\dot{\eta}_M(t) \tag{43}$$

Once again, comparison with the experimental results requires obtaining the absolute tip velocity response (relative to the fixed reference frame). Therefore, the velocity of the moving base is first computed from the base acceleration history by analytically integrating Eq. (40) and assuming $p_0 = 0$ (zero mean value for the base acceleration):

$$\dot{w}_{base}(t) \cong \sum_{k=1}^{N}\left[\frac{p_k T}{2\pi k}\sin\left(k\frac{2\pi t}{T}\right) - \frac{q_k T}{2\pi k}\cos\left(k\frac{2\pi t}{T}\right)\right] \tag{44}$$

Superposing the time history of the base velocity to the relative tip velocity, the absolute tip velocity is obtained and its mean-square value can be calculated using

$$E[\dot{w}^2(L,t)] = \frac{1}{T}\int_0^T \dot{w}^2(L,t)dt = {\sigma_{\dot{w}}}^2 \tag{45}$$

where $\sigma_{\dot{w}}$ is the standard deviation of the absolute tip velocity of the cantilever.

3.4.2 Euler-Maruyama solution

An alternative approach for the solution of Eq. (39) is to treat the problem as a set of stochastic differential equations (SDEs) and to use the Euler-Maruyama method [42] as done by Ferrari et al. [27] and Litak et al. [15], among others, for the SDOF problem, which is extended to cover multiple vibration modes here.

The voltage output and modal velocities are approximated by using Euler-Maruyama scheme [42]:

$$\begin{bmatrix} du_1^{(1)} \\ du_2^{(1)} \\ \vdots \\ du_M^{(1)} \\ du_1^{(2)} \\ du_2^{(2)} \\ \vdots \\ du_M^{(2)} \\ du^{(3)} \end{bmatrix} = \begin{bmatrix} u_1^{(2)} \\ u_2^{(2)} \\ \vdots \\ u_M^{(2)} \\ -2\zeta_1\omega_1 u_1^{(2)} - {\omega_1}^2 u_1^{(1)} + \tilde{\theta}_1 u^{(3)} \\ -2\zeta_2\omega_2 u_2^{(2)} - {\omega_2}^2 u_2^{(1)} + \tilde{\theta}_2 u^{(3)} \\ \vdots \\ -2\zeta_M\omega_M u_M^{(2)} - {\omega_M}^2 u_M^{(1)} + \tilde{\theta}_M u^{(3)} \\ -u^{(3)}/R_l C_p^{eq} - \tilde{\theta}_1 u_1^{(2)}/C_p^{eq} - \tilde{\theta}_2 u_2^{(2)}/C_p^{eq} - \cdots - \tilde{\theta}_M u_M^{(2)}/C_p^{eq} \end{bmatrix} dt + \begin{bmatrix} 0 \\ 0 \\ \vdots \\ 0 \\ \sigma_1 \\ \sigma_2 \\ \vdots \\ \sigma_M \\ 0 \end{bmatrix} dW \tag{46}$$

where dW is the increment of Wiener process and is approximated as

$$dW = a(t)dt \tag{47}$$

Since the Euler-Maruyama method requires a very fine time increment, the original time history of excitation input $a(t)$ is interpolated using a much higher sampling frequency of about 1 MHz (as compared to the original sampling frequency of 2560 Hz in the following experiments). The interpolated acceleration history is then checked to ensure that its standard deviation and mean remain the same as the original history. Following the Euler-Maruyama scheme, after obtaining the time histories of voltage and modal coordinates, the expected value of power output can be computed using Eq. (42), and the time history of tip velocity relative to moving base can be computed using Eq. (43). In order to obtain the absolute tip velocity (relative to the fixed reference frame), we again use the Fourier series representation of the velocity of the base, as done in previous section. The base velocity is also interpolated (and checked for its mean and standard deviation) and then superimposed to the relative tip velocity, and the mean-square value of the absolute tip velocity is calculated using Eq. (45).

3.5 Experimental validation

3.5.1 Experimental setup and cantilevered bimorph

A brass-reinforced PZT-5H piezoelectric bimorph (T226-H4-103X by Piezo Systems Inc.) is employed for the model validation experiments. In the experimental setup (Fig. 3), the bimorph is clamped at one end (shaker side) and free at the other end. The bimorph cantilever (Fig. 4a) is composed of two PZT-5H layers (with thin nickel electrodes covering the transverse faces) bracketing a brass layer as shown in the close-up side view photo of Fig. 4b and its basic

properties are listed in Table 2. The brass layer provides the electrical conductivity between the inner electrodes of the oppositely poled PZT-5H layers, and therefore the configuration employs the series connection of the piezoelectric layers (Fig. 2a). An accelerometer is attached on the top surface of the aluminum clamp and the clamp is attached onto the armature of an electromechanical shaker. Since the clamp is assumed to behave like a rigid body in the frequency range of interest, the accelerometer measures the base acceleration, $a(t)$. A laser vibrometer measures the tip velocity in the lateral (vertical) direction. A resistor box is connected to the electrode terminals of the bimorph and voltage across the electrical load is measured for several resistance values ranging from the short-circuit to open-circuit conditions. Three input channels of the data acquisition system are used. The first channel (the reference channel) records the acceleration processed by a signal conditioner, the second channel records the voltage measured across the resistive load, and the third channel measures the tip velocity measured by the laser vibrometer.

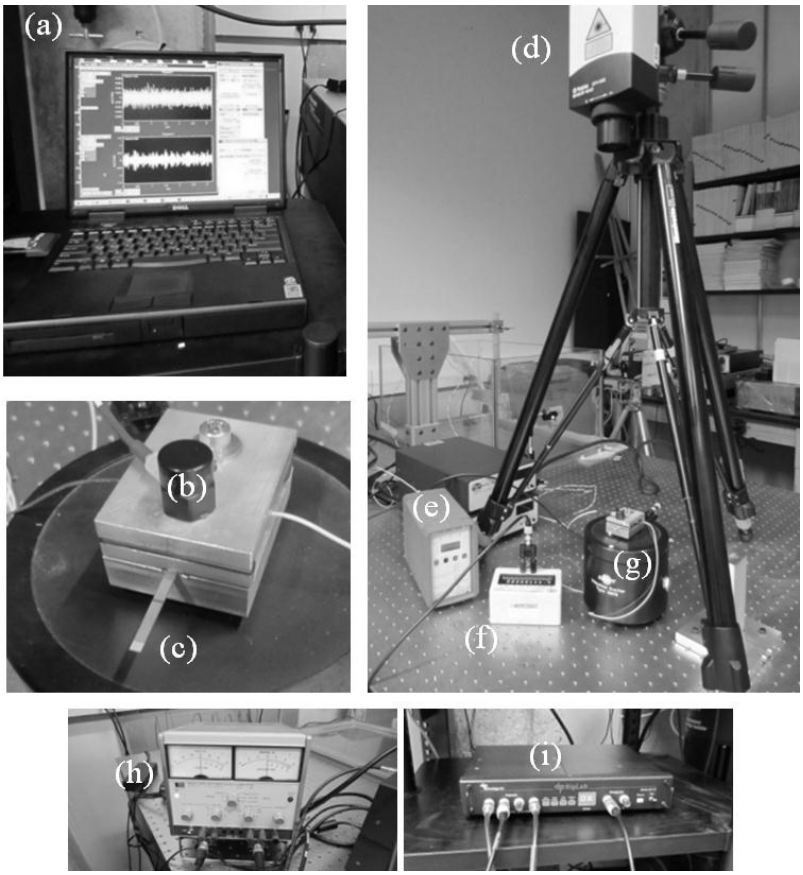

Figure 3. Details of the experimental setup: (a) computer with data acquisition software; (b) accelerometer on the clamp mounted to the armature of the shaker; (c) piezoelectric bimorph cantilever; (d) laser vibrometer; (e) signal conditioner; (f) resistor box; (g) shaker; (h) power supply/amplifier; and (i) data acquisition hardware.

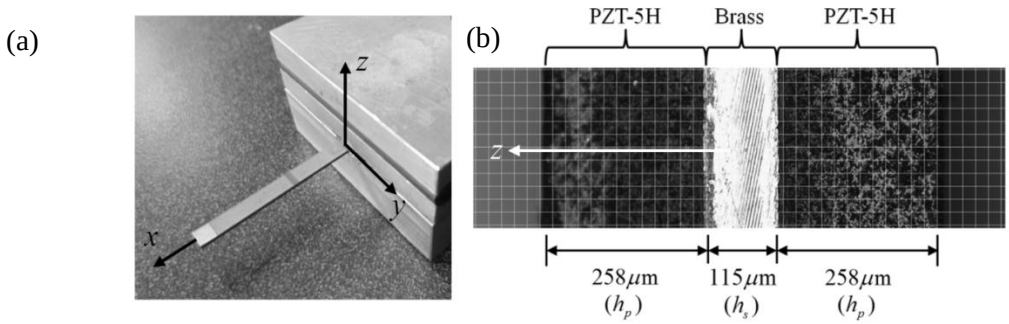

Figure 4. (a) Close-up view of the brass-reinforced cantilevered bimorph shown in Fig. 3c and (b) its side view displaying the thicknesses of piezoelectric and substructure layers. The brass layer provides the electrical conductivity between the inner electrodes of the oppositely poled piezoelectric layers.

Table 2. Geometric and material properties of the PZT-5H bimorph cantilever used in experiments

	Piezoceramic (PZT-5H)	Substructure (brass)
Length [mm]	27	27
Width [mm]	3.2	3.2
Thickness [mm]	0.258 (each)	0.115
Mass density [kg/m^3]	7500	9000
Elastic modulus [GPa]	60.6	105
Piezoelectric constant [C/m^2]	-16.6	–
Permittivity constant [nF/m]	25.55	–

3.5.2 Experimental validation of electroelastic FRFs

Prior to the broadband random vibration experiments, low-amplitude chirp excitation tests are conducted for the purpose of obtaining the linear electroelastic response FRFs of the system. Figure 5 shows that the analytical voltage and tip velocity FRFs are in very good agreement with the experimental results for a set of resistors ranging from short-circuit to open-circuit conditions. Note that the base acceleration in these FRFs is given in terms of the gravitational acceleration, g = 9.81 m/s^2. Close-up views around the fundamental vibration mode are also displayed in these figures, verifying the accuracy of the distributed-parameter model in predicting the shift in the fundamental resonance frequency with changing load resistance. Recall that the analytical multi-mode FRFs are due to Eqs. (13) and (36) for the voltage and the absolute velocity response, respectively. The modal mechanical damping ratios of the first and the second modes covered in the experimental measurements are obtained as 0.64 % and 0.75 %, respectively, i.e., $\zeta_1 = 0.0064$ and $\zeta_2 = 0.0075$. It is important to note that these are the purely mechanical damping ratios in the absence of electrical (shunt) damping. Typically, it is convenient to identify these damping ratios in short-circuit or open-circuit conditions if conventional methods (half-power points, logarithmic decrement, etc.) [40] are to be used instead of electromechanical identification expressions in the presence of finite shunt resistance [19].

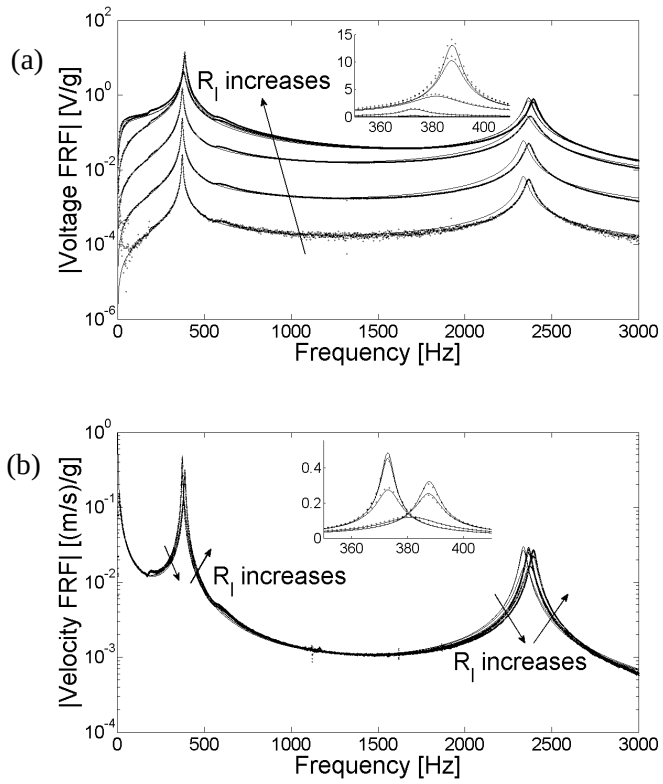

Figure 5. Experimental validation of the electroelastic FRFs: (a) voltage and (b) tip velocity FRFs of the PZT-5H bimorph for a set of resistors. Solid lines are the analytical predictions and dots are the experimental measurements.

The extension of the analytical FRF simulations to cover the frequency range of 0-10 kHz (hence the first three vibration modes) is shown in Fig. 6, where the damping ratios for mode 3 as well as higher modes which are outside the range of 0-10 kHz are calculated by using the identified damping ratios of the first two modes in the proportional (Rayleigh) damping equations [38, 43]. Having validated the electroelastic FRFs of the system, broadband random excitation experiments are conducted next.

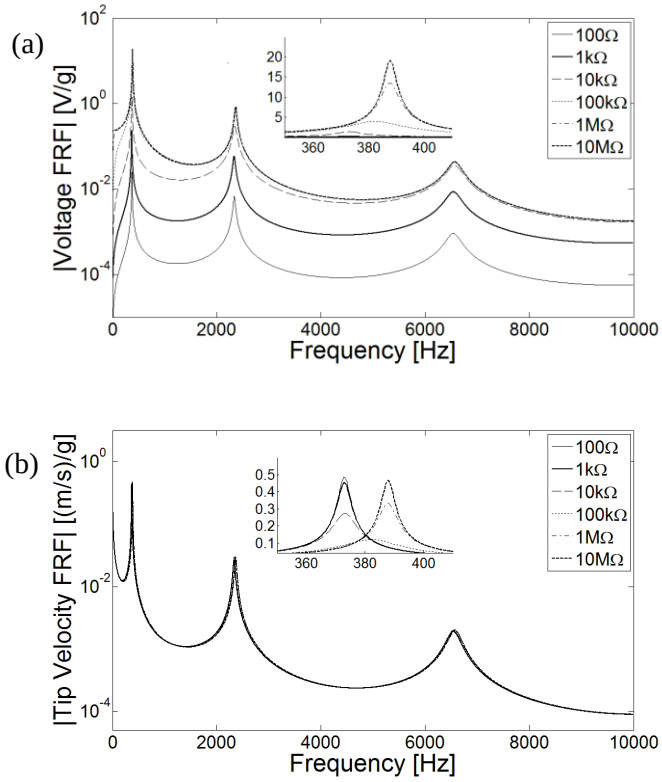

Figure 6. Analytically obtained (a) voltage and (b) tip velocity FRFs of the PZT-5H bimorph for a set of resistors in the frequency range of 0-10 kHz.

3.5.3 Broadband random excitation

In the random excitation experiments, the base excitation is intended to cover a broad range of excitation frequencies to be as close to white noise as possible within the limitations of the electromechanical shaker and other hardware. A sample of time history of acceleration in a broadband random excitation test is shown in Fig. 7 along with its PSD. Several experiments (not discussed here) show that the PSD of base acceleration is fairly flat up to 3 kHz (which covers the first two vibration modes of the harvester) and gradually decays above this value due to device (mainly shaker) limitations although the software used in signal generation is theoretically capable of feeding signal input up to 20 kHz.

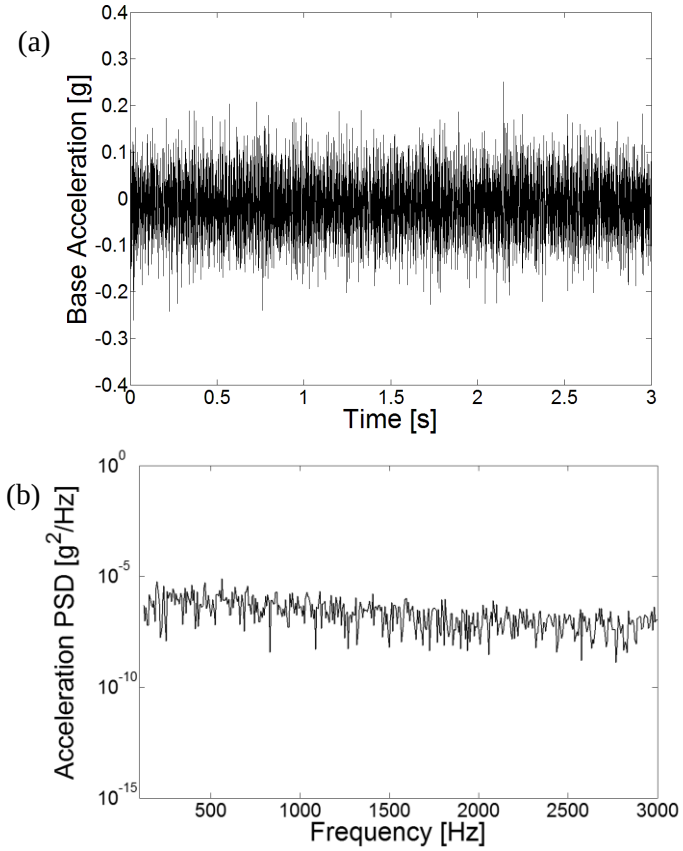

Figure 7. (a) A sample of time history of the measured random base acceleration (approximate PSD: $1.7(\mathrm{m}g)^2/\mathrm{Hz}$) and (b) its PSD for a broad frequency range.

A resistor sweep from $500\,\Omega$ (close to short-circuit condition) to $1\,\mathrm{M}\Omega$ (close to open-circuit condition) is performed. In each set of experiments, base acceleration, voltage output, and tip velocity are recorded for 3.2 seconds. For each resistive load, the test is repeated five times. From Eqs. (42) and (45), the expected (mean) power and mean-square tip velocity are computed. The same experimental procedure is repeated for three different excitation levels send to the shaker. While the data acquisition system (SigLab) extracts the PSD of base acceleration, we also estimate this PSD from the time history using the Welch method in MATLAB, which is a commonly used algorithm in PSD estimation. A sampling frequency of 2560 Hz is used in the estimation. Shown in Fig. 8 are the experimentally extracted PSD (from the data acquisition

system), the estimated PSD based on the Welch method, and the averaged PSD for the base acceleration history shown in Fig. 7.

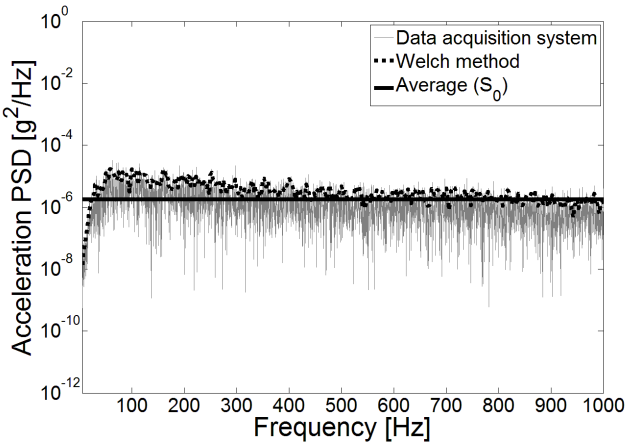

Figure 8. PSD of base acceleration shown in Fig. 7 extracted directly from the data acquisition system, estimated using the Welch method, and averaged based on the Welch estimate.

In the analytical solution, the base excitation is assumed to be ideal Gaussian white noise with a constant PSD, S_0. In order to obtain the constant value of S_0, the relatively flat portion of the Welch estimate is used and an average value is extracted. For instance, using the Welch estimate shown in Fig. 8, we identify $S_0 = 1.7(\text{m}g)^2/\text{Hz}$ for the base acceleration history given in Fig. 7. This estimation is performed for the time history of base acceleration in each of the tests and the mean values are obtained. As shown in Fig. 9 for 70 different time series for each PSD level (14 different resistors and 5 time series at each level), it can be concluded that the shaker generates excitations with good consistency in the base acceleration PSD. Therefore, it is reasonable to use the mean PSD in the analytical solution for all resistance values while the individual time histories are used in the ODE-based and SDE-based numerical solutions toward predicting the expected value of the electrical power and mean-square value of the shunted vibration response.

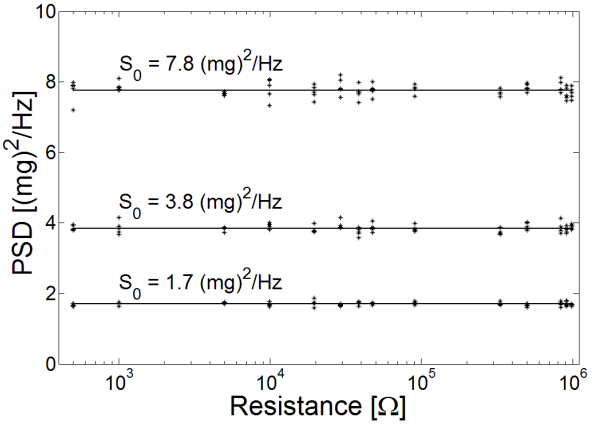

Figure 9. PSD values estimated from the Welch algorithm for all tests at three base excitation levels ($1.7,\ 3.8,$ and $7.8\ (\mathrm{m}g)^2/\mathrm{Hz}$) along with the average PSD values at each level (a total of 210 different time series).

3.5.4 Expected value of the electrical power output

At each level of base excitation, the experimental measurements are plotted and compared against the analytical and numerical predictions. An example case is given in Fig. 10a for the excitation PSD level of $1.7(\mathrm{m}g)^2/\mathrm{Hz}$. Very good agreement is observed between the experimental results and model predictions (both analytical and numerical). The difference between single-mode and multi-mode analytical solutions is due to the effect of higher vibration modes considering the lightly damped nature of the second vibration mode (see Fig. 5). Both numerical solutions employ only the first vibration mode to minimize the computational time while the analytical solutions can easily include several vibration modes (10 modes are used in the simulations). The analytical solutions use the frequency-domain integration range of [-10 kHz, 10 kHz], i.e., $\bar{\omega} = 10\,\mathrm{kHz}$ in section 3.3. It is also important to note that, in the analytical predictions, an average value of PSD is used for all resistors. However, in each of the numerical simulations, the respective time history of base acceleration is directly employed as the input.

Consequently, at each value of electrical resistance, the Fourier series-based ODE solution and the SDE solution based on the Euler-Maruyama method (as well as the experimental measurements) have five different data points in Fig. 10a. Note that, one can easily take the averages of the experimental and numerical data points of five separate random data series at each resistor to simplify Fig. 10a to Fig. 10b for clarity.

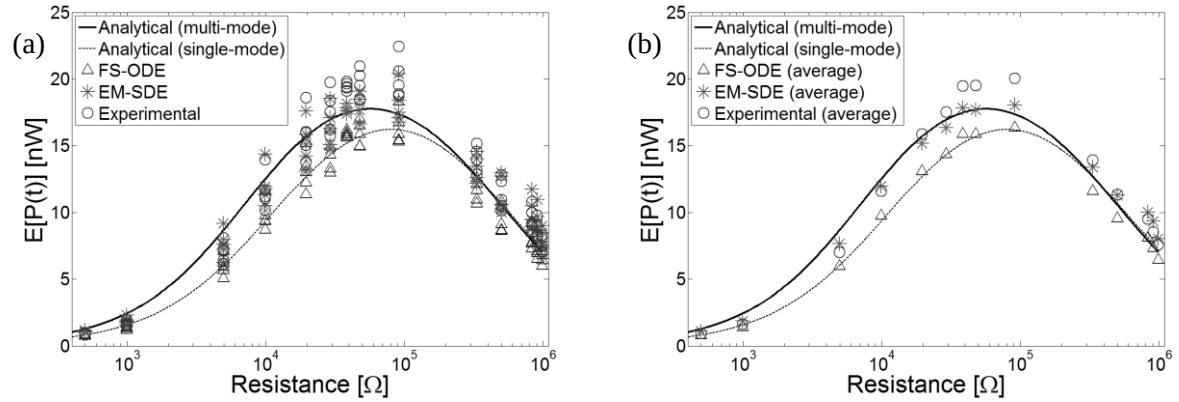

Figure 10. Comparison of the analytical and numerical simulations of mean power output with the experimental measurements for a set of resistive loads showing (a) five experimental and numerical data points at each resistor and (b) only average values for clarity (PSD level of base acceleration: $1.7(\mathrm{m}g)^2/\mathrm{Hz}$). In the legends, the Fourier series-based ODE solution is denoted by FS-ODE while the SDE solution based on the Euler-Maruyama scheme is denoted by EM-SDE.

The analytical predictions, numerical simulations, and experimental measurements for three levels of base acceleration PSD are plotted in Fig. 11a (and the version based on averaging the numerical and experimental data points at each resistor is shown in Fig. 11b). The base excitation levels are represented in terms of their averaged PSD values following Fig. 9. Both the analytical and numerical predictions of the expected power exhibit very good agreement with the experimental results. The multi-mode analytical solution more accurately predicts the experimental results around the optimal resistance region at each PSD level. It should be noted that the horizontal axis is in logarithmic scale and the optimal electrical load in the single-mode

and multi-mode analytical predictions are substantially different although the amplitude-wise difference is relatively small.

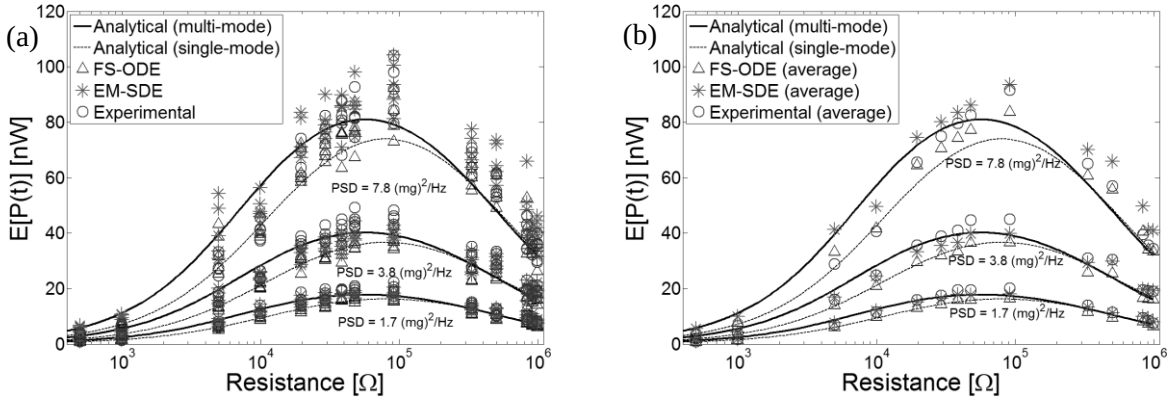

Figure 11. Comparison of the analytical and numerical simulations of mean power output with the experimental measurements for a set of resistive loads at different PSD levels of base acceleration ($1.7,\ 3.8,$ and $7.8\ (\mathrm{m}g)^2/\mathrm{Hz}$) showing (a) five experimental and numerical data points at each resistor and (b) only average values for clarity. In the legends, the Fourier series-based ODE solution is denoted by FS-ODE while the SDE solution based on the Euler-Maruyama scheme is denoted by EM-SDE.

In addition, a hybrid solution which uses the information of analytical FRFs of the system and the experimental PSD is computed. Recall Eq (28), instead of taking PSD of base excitation as a constant, S_0, the PSD measured directly by the data acquisition system is employed.

$$E\left[P(t)\right] = \int_{-\bar{\omega}}^{\bar{\omega}} \frac{S(\omega)}{R_l} \left|\alpha(\omega)\right|^2 d\omega \tag{48}$$

Where $S(\omega)$ is the PSD of the base acceleration measured by the data acquisition system, $[-\bar{\omega}, \bar{\omega}]$ is the frequency boundary of the PSD, and $\alpha(\omega)$ is the voltage output – to – base acceleration FRF. Figure 12 presents the comparison of this solution and the experimental results, and very accurate predictions of this solution are observed. The purpose of presenting this

solution is to demonstrate that given any PSD of a random excitation and the FRFs of an energy harvester, its power generation can be accurately predicted using Eq (48).

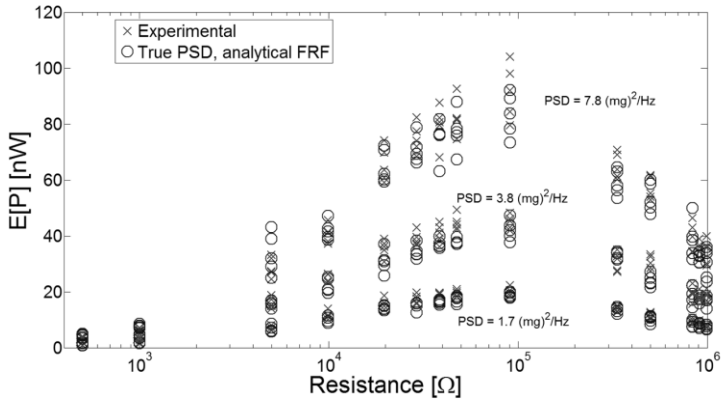

Figure 12. Comparison of the experimental results and a hybrid analytical solution of mean power output for a set of resistive loads at different PSD levels of base acceleration ($1.7,\ 3.8,$ and $7.8\ (\mathrm{m}g)^2/\mathrm{Hz}$).

3.5.5 Mean-square value of the shunted vibration response

The single-mode and multi-mode analytical, numerical, and experimental results of the tip velocity at excitation level of $1.7(\mathrm{m}g)^2/\mathrm{Hz}$ are compared in Fig. 13. As in the case of power generation, the analytical and numerical simulations of the tip velocity response match very well with experimental results. The mean-square of vibration response is observed to be relatively insensitive to the higher-mode effects. Comparisons across different excitation levels are summarized in Fig. 14 with very good predictions particularly around the optimal loads of the maximum power output and minimum vibration response.

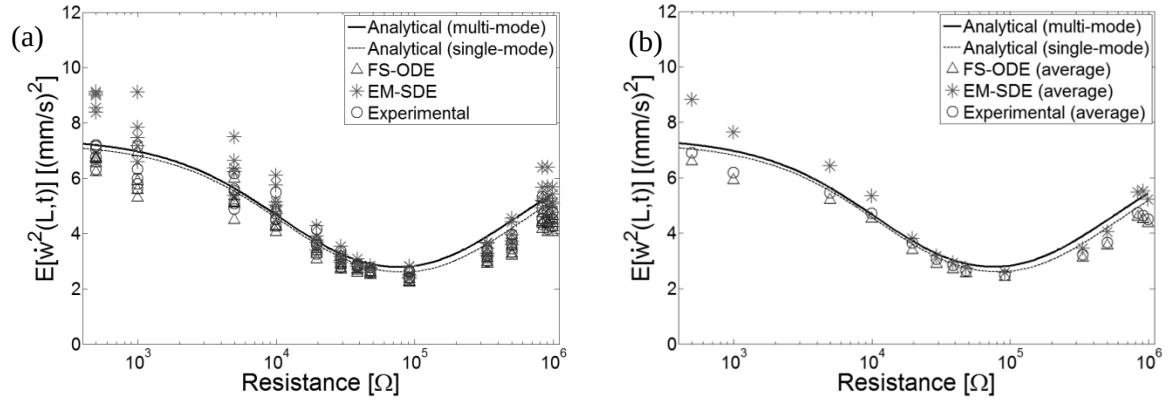

Figure 13. Comparison of the analytical and numerical simulations of mean-square shunted tip velocity with the experimental measurements for a set of resistive loads showing (a) five experimental and numerical data points at each resistor and (b) only average values for clarity (PSD level of base acceleration: $1.7(\mathrm{m}g)^2/\mathrm{Hz}$). In the legends, the Fourier series-based ODE solution is denoted by FS-ODE while the SDE solution based on the Euler-Maruyama scheme is denoted by EM-SDE.

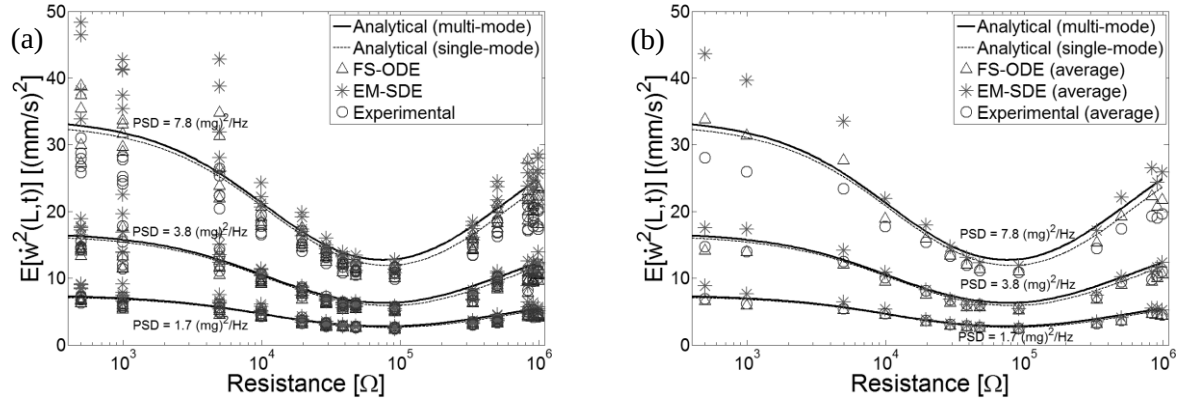

Figure 14. Comparison of the analytical and numerical simulations of mean-square shunted tip velocity with the experimental measurements for a set of resistive loads at different PSD levels of base acceleration ($1.7,\ 3.8,$ and $7.8\ (\mathrm{m}g)^2/\mathrm{Hz}$) showing (a) five experimental and numerical data points at each resistor and (b) only average values for clarity. In the legends, the Fourier series-based ODE solution is denoted by FS-ODE while the SDE solution based on the Euler-Maruyama scheme is denoted by EM-SDE.

Furthermore, the hybrid solution which uses analytical FRFs of the system and the experimental PSD is computed. By replacing the constant PSD, S_0, with the actual PSD, $S(\omega)$, measured directly by the data acquisition in Eq (35), we obtain

$$E\left[\dot{w}^2(L,t)\right] = \int_{-\infty}^{\infty} S(\omega)\left|\beta^{modified}(\omega,L)\right|^2 d\omega \tag{49}$$

Where $S(\omega)$ is the measured PSD of the base acceleration, $[-\bar{\omega},\bar{\omega}]$ is the frequency boundary of the PSD, and $\beta^{modified}(\omega,L)$ is the tip velocity – to – base acceleration FRF. Figure 15 presents the comparison of this solution and the experimental results, and shows that this solution can predict results very well.

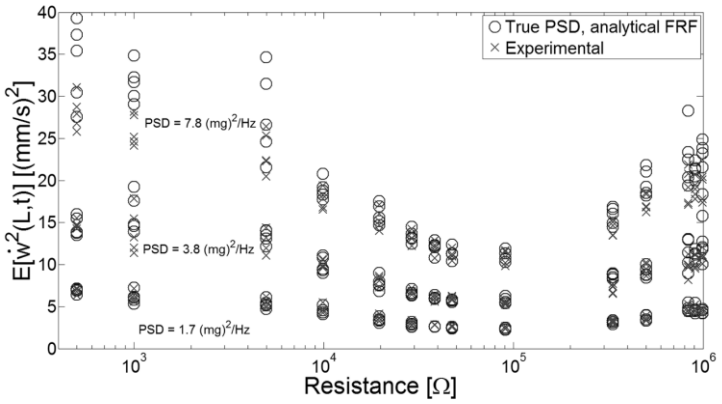

Figure 15. Comparison of the experimental results and a hybrid analytical solution of mean-square shunted tip velocity for a set of resistive loads at different PSD levels of base acceleration ($1.7,\ 3.8,$ and $7.8\ (\text{m}g)^2/\text{Hz}$).

The maximum expected power output and the minimum mean-square tip velocity response versus input PSD are plotted in Figs. 16a and 16b, respectively. We recall that the analytical solutions for the expected power and mean-square tip velocity are due to Eqs. (21) and (35), respectively, where the proportionality of the left hand side (mean power or mean-square

tip velocity) to the input PSD is evident for the case of white noise excitation since the S_0 term can be taken outside the integral.

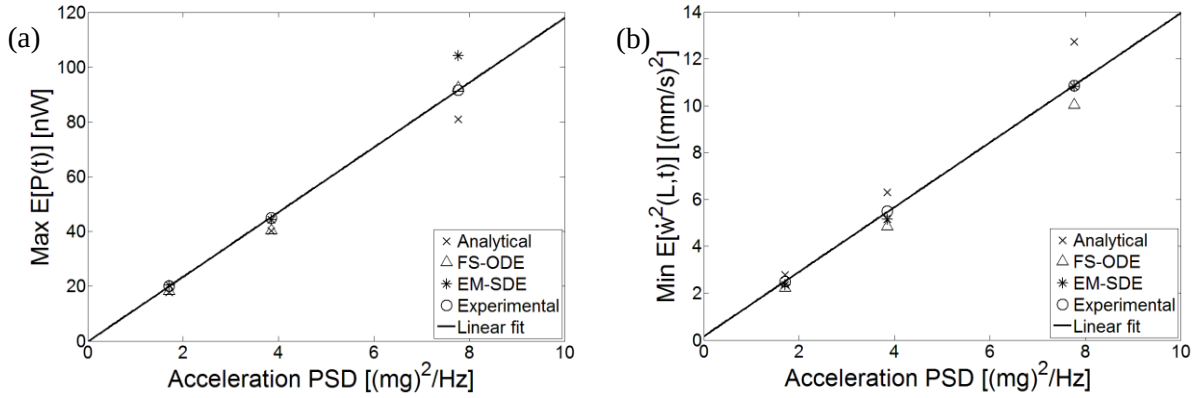

Figure. 16. (a) Maximum expected power output and (b) minimum mean-square shunted tip velocity at different levels of base acceleration PSD exhibiting linear dependence between the maximum expected power, minimum mean-square tip velocity, and base acceleration PSD.

3.6 Comparison of various piezoelectric materials

In this section, a theoretical case study of energy harvesting from broadband random excitation is presented for various piezoelectric materials: PZT-5H, PZT-8, PMN-PZT, PMN-PZT-Mn. The piezoelectric bimorphs share the same geometric properties with the bimorph investigated in the previous section and the same brass layer is assumed (see Table 2). The relevant material properties are given in Table 3 [44,45].

PZT-5H is a soft ceramic with larger piezoelectric strain constant (d_{31}) and smaller mechanical quality factor (Q_m) whereas PZT-8 is a hard ceramic with smaller piezoelectric constant and larger mechanical quality factor. PMN-PZT is a soft single-crystal with larger piezoelectric strain constant and smaller mechanical quality factor compared to PMN-PZT-Mn, which is a hard single crystal. It is assumed that the entire mechanical loss of each bimorph is

due to its mechanical quality factor. Therefore, the dissipative effects of external damping and clamping conditions are assumed to be identical (and negligible) so that the active materials can be compared under the same conditions by considering their internal mechanical loss only. The damping ratio of the fundamental mode ($\zeta_1 \cong 1/2Q_m$) for each cantilever is given in Table 4. The same damping ratio is assumed for the higher vibration modes of the respective cantilevers. First, the analytical FRFs are generated, and then expected power and mean square of tip velocity are computed. The broadband random excitation is assumed to be ideal Gaussian white noise.

Table 3**.** Elastic, piezoelectric, and dielectric properties of the materials ($\bar{e}_{31} = d_{31} / s_{11}^E$, $\bar{\varepsilon}_{33}^S = \varepsilon_{33}^T - d_{31}^2 / s_{11}^E$).

	PZT-5H	**PZT-8**	**PMN-PZT**	**PMN-PZT-Mn**
d_{31} [pm/V]	-274	-97	-718	-513
s_{11}^E [pm^2/N]	16.4	11.5	62.0	42.6
$\varepsilon_{33}^T / \varepsilon_0$	3400	1000	4850	3410
$\bar{e}_{31}$ [C/m^2]	-16.7	-8.4	-11.6	-12.0
$\bar{\varepsilon}_{33}^S$ [nF/m]	25.5	8.0	34.6	24.0
Q_m	65	1000	100	1050

Table 4. Mechanical damping ratio for the fundamental vibration mode of each bimorph cantilever.

Cantilever type	$\zeta_1 \cong 1/2Q_m$
PZT-5H	0.77 %
PZT-8	0.050 %
PMN-PZT	0.50 %
PMN-PZT-Mn	0.0476 %

3.6.1 Electroelastic FRFs

The analytical FRFs of four different piezoelectric materials are plotted in Figs. 17-20. Due to its larger elastic compliance, the PMN-PZT bimorph and PMN-PZT-Mn have lower resonance frequencies. Bimorphs made of hard materials PZT-8 and PMN-PZT-Mn have lighter damping, which results in sharper peaks at resonance.

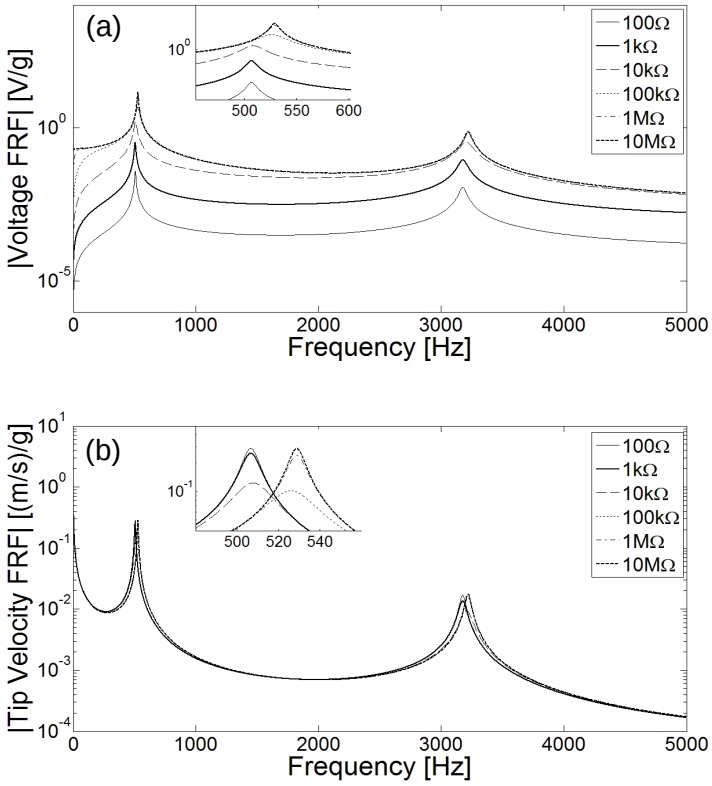

Figure 17. (a) Voltage – to – base acceleration FRFs and (b) tip velocity – to – base acceleration FRFs of the PZT-5H bimorph for a set of resistors.

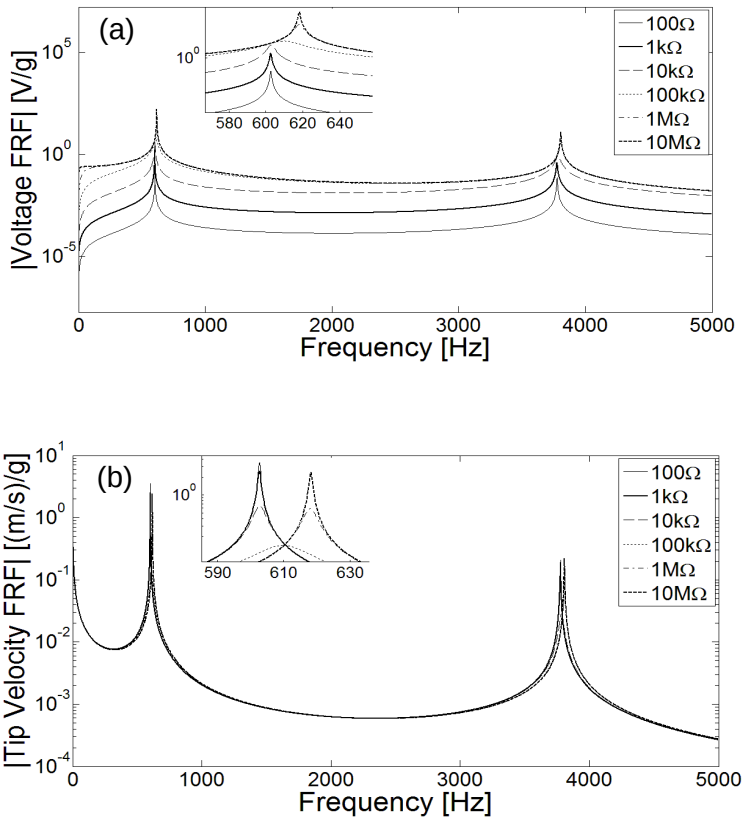

Figure 18. (a) Voltage – to – base acceleration FRFs and (b) tip velocity – to – base acceleration FRFs of the PZT-8 bimorph for a set of resistors.

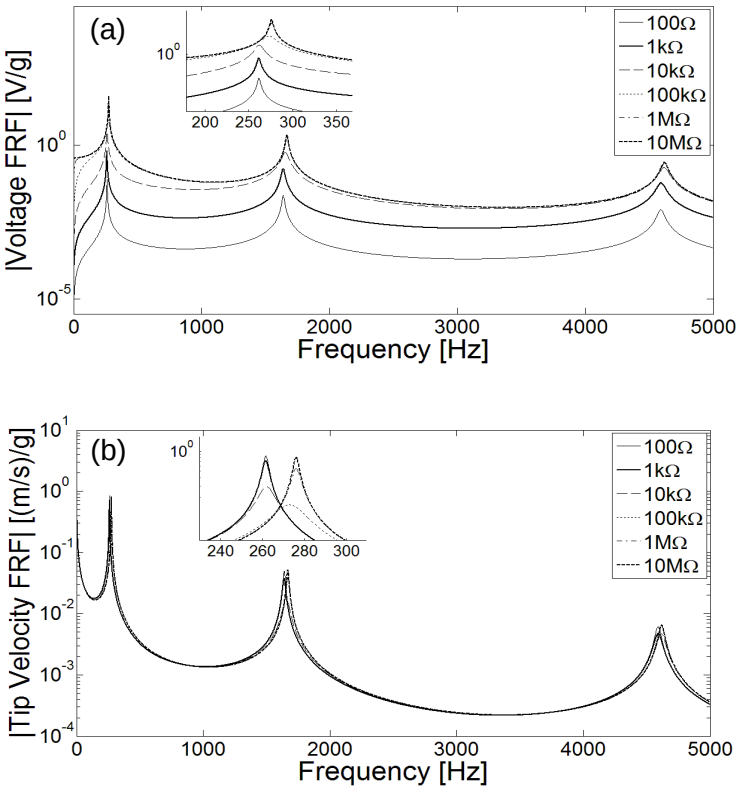

Figure 19. (a) Voltage – to – base acceleration FRFs and (b) tip velocity – to – base acceleration FRFs of the PMN-PZT bimorph for a set of resistors.

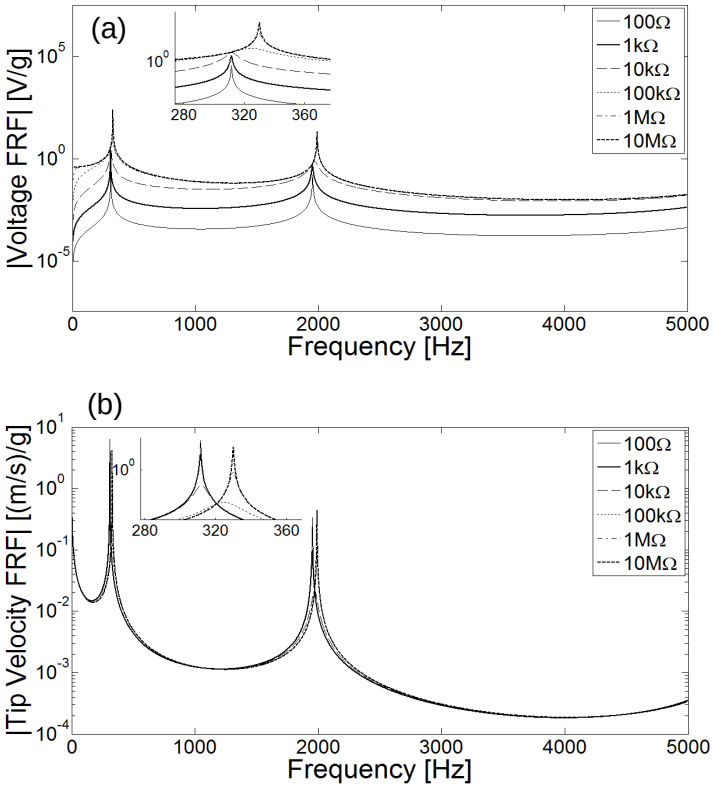

Figure 20. (a) Voltage – to – base acceleration FRFs and (b) tip velocity – to – base acceleration FRFs of the PMN-PZT-Mn bimorph for a set of resistors.

3.6.2 Expected value of the electrical power output

As shown in Fig. 21, PMN-PZT-Mn generates the largest power output from broadband random excitation, and it is followed by PZT-8, PMN-PZT, and PZT-5H. The maximum power PMN-PZT-Mn can generate is about 70% higher than the maximum power PZT-5H can generate. Following the same order, PMN-PZT-Mn has the largest flat region around the optimal resistance whereas PZT-5 has the narrowest region. Hard ceramic and single-crystal bimorphs are less sensitive to variations in the external load resistance, which might be preferred if the electrical load is not exactly known in the application. It is particularly important to note that the

performance difference between the materials is not by an order of magnitude (unlike harmonic excitation at resonance investigated by Erturk and Inman [38] for the same materials).

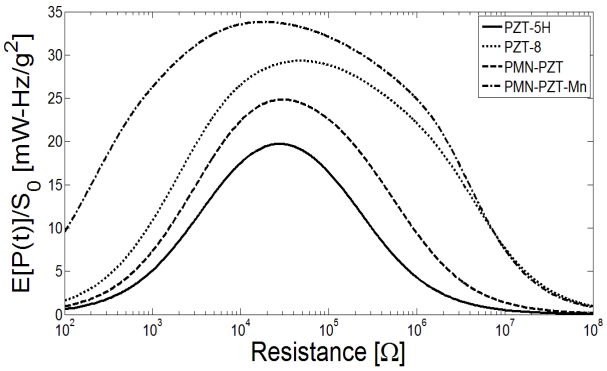

Figure 21. Expected power output for bimorphs made of different piezoelectric materials (from broadband random excitation).

3.6.3 Mean-square value of the vibration response

As far as the vibration response is concerned, the PMN-PZT-Mn and PZT-8 bimorphs exhibit the largest vibration attenuation (in the optimal resistance region) relative to their respective short-circuit vibration levels. This indicates that PMN-PZT-Mn and PZT-8 have larger shunt damping effect due to power generation from broadband random excitation (Fig. 22).

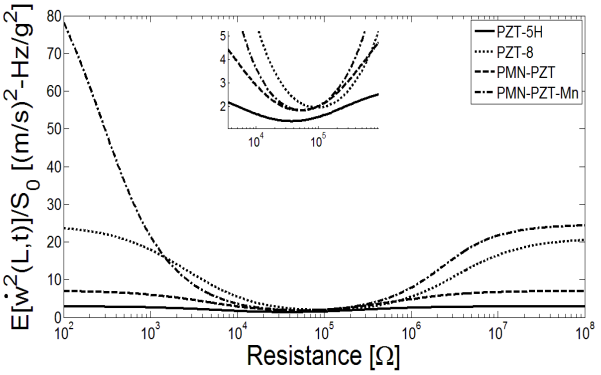

Figure 22. Mean square value of tip velocity for bimorphs made of different piezoelectric materials.

Combining the observations obtained from Figs. 21 and 22, one can conclude that hard ceramics perform better than soft ceramics while hard single crystals perform better than soft single crystals. In addition, hard ceramics (PZT-8) can outperform soft single crystals (PMN-PZT). Importantly, there is no substantial (i.e., order of magnitude) difference between the power outputs of the hard ceramic and single-crystal bimorphs. That is, bimorphs made of all four materials (soft and hard ceramics and crystals) result in power outputs on the same order of magnitude for the same broadband random vibrational input.

3.7 Conclusions

Analytical and numerical solutions, and experimental validations of piezoelectric energy harvesting from broadband random vibrations using cantilevered bimorphs are presented based on a distributed-parameter electroelastic model. The analytical solution uses the combination of distributed-parameter electroelastic FRFs with the input power spectral density (PSD) while the numerical solutions treat the random base excitation problem in two separate approaches deterministically and stochastically. The deterministic approach represents the base acceleration history in terms of its Fourier series expansion to use with the first-order electroelastic equations in an ordinary differential equation (ODE) solver while the stochastic approach directly employs an Euler-Maruyama scheme to solve the resulting first-order stochastic differential equations (SDEs). The expected (mean) piezoelectric power output and the mean-square vibration response forms are investigated for a broad range of resistive loads spanning from the short-circuit to open-circuit conditions. The shunt damping effect associated with random piezoelectric power generation is also reported. The analytical as well as ODE-based and SDE-based numerical predictions exhibit very good agreement with the experimental measurements taken for a brass-

reinforced PZT-5H piezoelectric energy harvester. The analytical and numerical solutions are further validated for different PSD levels of random excitation. It is observed that the expected power and mean-square vibration response depend on the input (base acceleration) PSD linearly. It can be concluded that the analytical and numerical solutions presented in this chapter are effective tools for predicting and optimizing the performance of cantilevered piezoelectric harvesters under broadband random excitation.

Based on the analytical solution, the effect of higher vibration modes is also investigated and it is concluded that lightly damped higher modes can alter the expected power curve (primarily the optimal load) if the PSD of input vibration covers high frequencies as in the case of white noise excitation.

Through theoretical studies, bimorphs made of four piezoelectric materials PZT-5H (soft ceramic), PZT-8 (hard ceramic), PMN-PZT (soft single crystal), PMN-PZT-Mn (hard single crystal) are compared for power generation under broadband random excitation. It is found that hard ceramics and single crystals outperform their soft counterparts. In addition, hard ceramics (PZT-8) can outperform soft single crystals (PMN-PZT). However, the power output levels are on the same order of magnitude unlike the case of resonant excitation from harmonic input.

CHAPTER 4

BROADBAND RANDOM EXCITATION OF A MULTILAYER STACK

4.1 Electroelastic modeling

Figure 23 shows a multilayer stack piezoelectric energy harvester configuration under pressure $p(t)$. The electrodes are connected to a resistive electrical load (R_l). Following the analytical modal analysis procedure, the governing ordinary differential equation is obtained as

$$C_p^{eq}\dot{v}(t)+\frac{1}{R_l}v(t)=d_{33}^{eff}A\dot{p}(t) \tag{50}$$

where C_p^{eq} is the equivalent capacitance, $v(t)$ is the voltage output of the system across the electrical load, d_{33}^{eff} is the effective piezoelectric constant, R_l is the external resistive load in the circuit, A is the cross-sectional area, $p(t)$ is the axial pressure (thus $F(t)=Ap(t)$ is the force exerted on the stack configuration), and $\dot{p}(t)$ is the time derivative of the pressure.

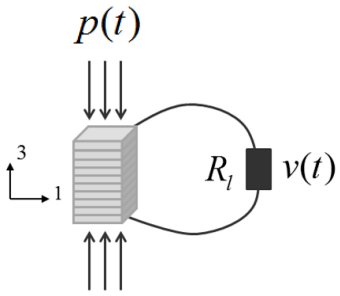

Figure 23. Schematic of a multilayer piezostack used for energy harvesting under random excitation.

If the pressure on the stack in Fig. 23 is harmonic of the form $p(t)=p_0e^{j\omega t}$ (where p_0 is the amplitude of the pressure, ω is the frequency and j is the unit imaginary number), hence,

the steady-state voltage response is $v(t) = Ve^{j\omega t}$ where V is the complex voltage that can be derived as

$$V = \frac{d_{33}^{eff} j\omega A p_o}{C_p^{eq} j\omega + \frac{1}{R_l}} \tag{51}$$

The voltage output – to – pressure input frequency response function (FRF) can be defined as

$$\alpha(\omega) = \frac{v(t)}{p_o e^{j\omega t}} = \frac{d_{33}^{eff} j\omega A}{C_p^{eq} j\omega + \frac{1}{R_l}} \tag{52}$$

The peak value of electrical power ($\tilde{P}(t)$) harvested using the stack under harmonic loading can then be expressed as

$$\left|\tilde{P}(t)\right| = \frac{V^2}{R_l} = \frac{(d_{33}^{eff} A p_o \omega)^2 R_l}{C_{\tilde{p}}^{eq2} \omega^2 R_l^{\,2} + 1} \tag{53}$$

The optimal electrical load (R_l^*) for maximum power output can be derived as

$$\frac{\partial}{\partial R_l}\left|\tilde{P}(t)\right|\Bigg|_{R_l = R_l^*} = 0 \rightarrow R_l^* = \frac{1}{C_p^{eq}\omega} \tag{54}$$

Back substitution into Eq. (53) leads to the following expression for maximum power output:

$$\tilde{P}_{\max} = \left|\tilde{P}(t)\right|_{R_l = R_l^*} = \frac{\omega d_{33}^{eff\,2} (A p_o)^2}{2C_p^{eq}} \tag{55}$$

4.2 Broadband random excitation: analytical solution

If we consider the axial pressure on the piezoelectric stack to be Gaussian white noise-type random signal, then it has a constant power spectral density (PSD) of S_0. That is, the input PSD covers the entire frequency band with constant amplitude. Using this property of the excitation and electroelastic FRF summarized in the previous section, the analytical solution to the expected (mean) power can be derived.

Recalling that the instantaneous electrical power output is simply $v^2(t)/R_l$, the expected value of the power output becomes [38]

$$E\left[\tilde{P}(t)\right] = \int_{-\infty}^{\infty} \frac{S_0}{R_l} \left|\alpha(\omega)\right|^2 d\omega \tag{56}$$

Therefore, the analytical solution for the expected power output is obtained from

$$E\left[\tilde{P}(t)\right] = \frac{S_0}{R_l} \int_{-\infty}^{\infty} \left| \frac{d_{33}^{eff} j\omega A}{C_p^{eq} j\omega + \frac{1}{R_l}} \right|^2 d\omega \tag{57}$$

Note that, when computing analytical solutions of stack energy harvester under band-limited random excitation (which is necessarily the case in the experiments), the frequency range is set to be $[-\bar{\omega}, \bar{\omega}]$ such that

$$E\left[\tilde{P}(t)\right] = \frac{1}{R_l} \int_{-\bar{\omega}}^{\bar{\omega}} S(\omega) \left|\alpha(\omega)\right|^2 d\omega \tag{58}$$

where $S(\omega)$ is the PSD of the excitation input and $\bar{\omega}$ is the upper frequency boundary of $S(\omega)$.

4.3 Broadband random excitation: numerical solutions

4.3.1 Fourier series-based Runge-Kutta solution

The first numerical solution approach treats the given time series of the excitation in a deterministic fashion through its Fourier series representation,

$$p(t) \cong m_0 + \sum_{k=1}^{N}\left[m_k \cos\left(k\frac{2\pi t}{T}\right) + n_k \sin\left(k\frac{2\pi t}{T}\right)\right] \tag{59}$$

where T is the length of the time history of the applied axial pressure, m_0 is its mean value, while m_k and n_k ($k = 1, 2, ...$ are positive integers) are the Fourier coefficients given by

$$m_0 = \frac{1}{T}\int_0^T p(t)dt\,,\ m_k = \frac{2}{T}\int_0^T p(t)\cos\left(k\frac{2\pi t}{T}\right)dt\,,\ n_k = \frac{2}{T}\int_0^T p(t)\sin\left(k\frac{2\pi t}{T}\right)dt \tag{60}$$

Thus the stochastic process is represented in a deterministic form and can be feed into the ordinary differential equation of the system:

$$\dot{v} = \frac{1}{C_p^{eq}}\left(d_{33}^{eff} A\dot{p} - \frac{1}{R_l}v\right) \tag{61}$$

where v is the voltage output, and $\dot{p}$ is the time derivative of the applied pressure along the axial direction. Note that zero initial conditions are assumed in the simulations).

The computation is carried out by using an ODE solver, such as the ode45 algorithm in MATLAB that uses an explicit Runge-Kutta formulation. The time history of the voltage output is obtained from the electroelastic ODE. If the pressure history has zero mean value, it is known

that the response forms also have zero mean value. Thus the expected value of power output can be computed by using

$$E\left[\tilde{P}(t)\right] = \frac{1}{T}\int_0^T \frac{v^2(t)}{R_l}\,dt = \frac{\sigma_v^{\,2}}{R_l} \tag{62}$$

where σ_v is the standard deviation of the voltage response.

4.3.2 Euler-Maruyama solution

An alternative approach for the solution of Eq. (61) is to treat the problem as a stochastic differential equation (SDE) and use the Euler-Maruyama method [42].

Using Euler-Maruyama scheme the voltage output is approximated by:

$$dv = -\frac{v}{R_l C_p^{eq}}\,dt + \frac{d_{33}^{eff} A}{C_p^{eq}}\,dW \tag{63}$$

Where v is the voltage response and dW is the increment of Wiener process. In this case dW is the increment of dynamic pressure exerted on the stack dp:

$$dW = dp \tag{64}$$

After obtaining the time history of voltage using Euler-Maruyama scheme, the expected value of power output can be computed using Eq. (62).

4.4 Experimental validation

4.4.1 Experimental setup and multilayer stack

A PZT-5H piezoelectric stack (TS18-H5-104 by Piezo Systems Inc.) is used in the experiments and its basic properties are listed in Table 5. In the experimental setup (Fig. 24), the stack is horizontally compressed by a long-stroke shaker which is capable of providing excitation at low frequencies. A force transducer is located between the stack and the moving armature of the shaker. A resistor box is connected to the electrode terminals of the stack and voltage across the electrical load is measured for several resistance values in order to capture the optimality of power output. Two input channels of the data acquisition system are used, one records the force processed by a signal conditioner, the other records the voltage measured across the resistive load.

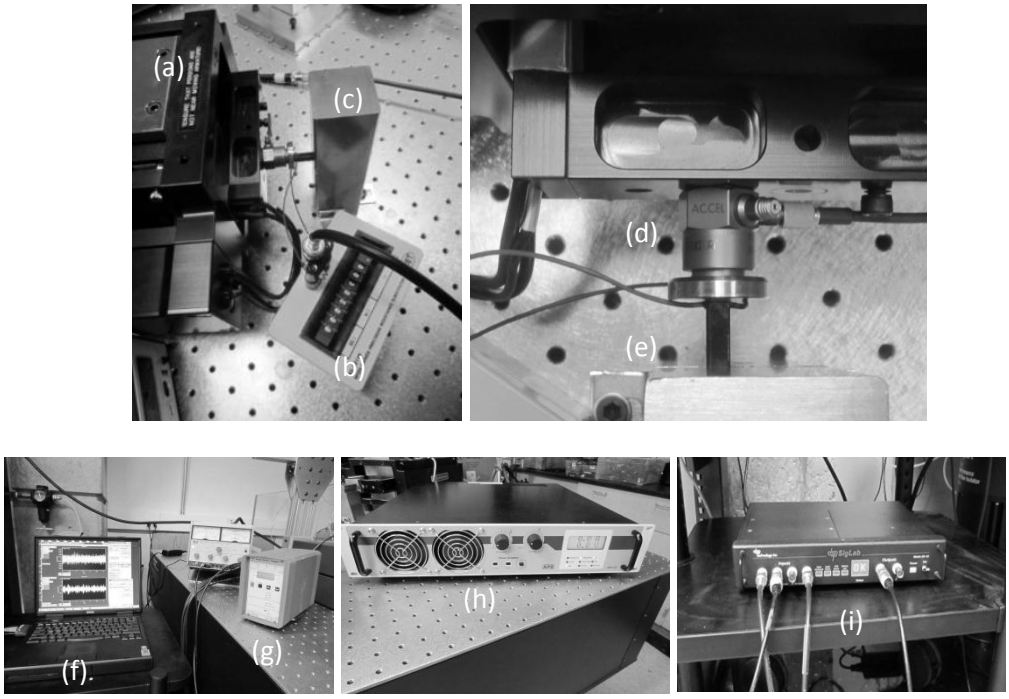

Figure 24. Experimental setup: (a) shaker; (b) resistor box; (c) stiff fixture; (d) force transducer; (e) piezoelectric stack; (f) computer with data acquisition software; (g) signal conditioner; (h) power amplifier for shaker; (i) data acquisition hardware.

Table 5. Geometric and material properties of the PZT-5H stack used in experiments

	Piezoceramic (PZT-5H)
L x W x H [mm]	5x5x18
d_{33} [pm/V]	650
d_{33}^{eff} [nm/V]	110.49
$\varepsilon_{33}^{T} / \varepsilon_{0}$	3800
C_{p} [nF]	1745

4.4.2 Experimental validation of electroelastic FRFs

Prior to the harmonic and random vibration experiments, chirp tests are conducted for the purpose of obtaining the electroelastic response FRFs of the system. Figure 25 shows that the analytical voltage output FRFs are in very good agreement with the experimental results for a set of resistors. The experimental FRF measurements focus on the low-frequency (non-resonance) range only. Having validated the electroelastic FRFs of the system, harmonic and random vibration experiments are conducted next.

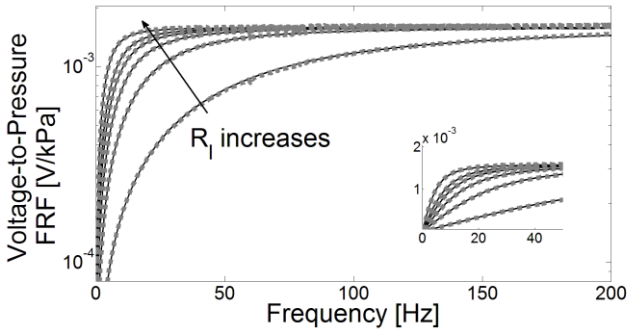

Figure 25. Voltage – to – pressure FRFs of the PZT-5H stack for a set of resistors (R_l =999, 2991, 4975, 6951, 8920, 14778 Ω). Solid lines are analytical predictions and dots are experimental measurements.

4.4.3 Harmonic excitation

The objectives of performing harmonic excitation experiments are to validate the analytical model and to determine the effective piezoelectric constant (d_{33}^{eff}) using

$$d_{33}^{eff} = \sqrt{\frac{2C_p^{eq}\tilde{P}_{\max}}{\omega(Ap_o)^2}} \tag{65}$$

which is derived from Eq (55). Here, C_p^{eq} is equivalent capacitance, $\tilde{P}_{\max}$ is maximum power, ω is excitation frequency, A is cross-sectional area and p_o is amplitude of applied axial pressure. The effective piezoelectric constant is determined using one experimental case and is successfully validated through all other cases.

In harmonic excitation experiments, the stack is subjected to harmonic excitation at three excitation frequencies: 10 Hz, 20 Hz, and 30 Hz. At each frequency, the stack is compressed by harmonic force with five different amplitudes, resulting in five pressure levels. A resistive sweep is performed in order to capture the optimality of power generation. The experimental measurements of harvested power are compared to analytical solutions computed using Eq (53).

For harmonic excitation at 20 Hz, the comparisons are shown in Fig 26. The power output normalized with respect to input pressure is shown in Fig 27.

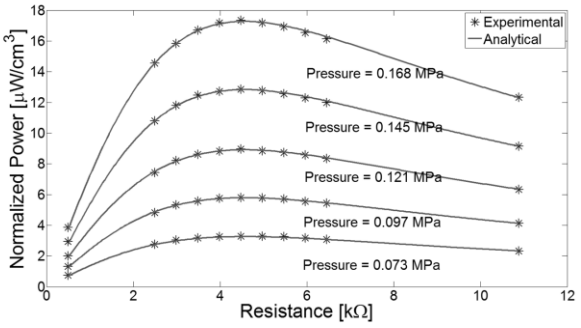

Figure 26. Peak value of power output (normalized with respect to the stack volume) under harmonic excitation at 20 Hz at different pressure levels.

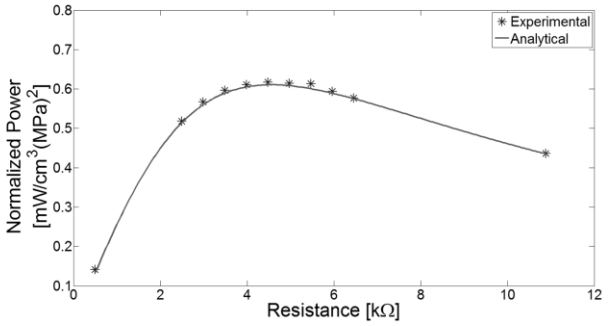

Figure 27. Peak value of power output (normalized with respect to the stack volume and input pressure) under harmonic excitation at 20 Hz.

To see the relation between input pressure and maximum output power, the maximum power is plotted with respect to amplitude of pressure (Fig 28). The analytical solutions and experimental measurements show very good agreement. As can be explained by Eq. (55), the maximum power output increases quadratically with amplitude of input force or pressure.

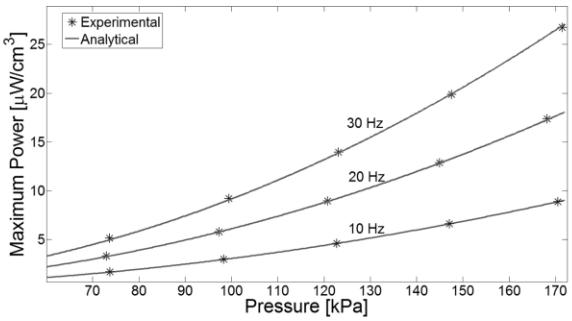

Figure 28. Maximum power output (normalized with respect to the stack volume and input pressure) under harmonic excitation at 10 Hz, 20 Hz and 30 Hz.

4.4.4 Broadband random excitation

The fundamental resonance frequency of the PZT-5H piezostack used in the experiments is 74 kHz according to the manufacturer (Piezo Systems Inc.). Therefore, all practical excitation frequencies are within the off-resonant quasistatic region of the stack. The random excitation provided in experiments has a bandwidth from 0 to 200Hz, which is considered as broadband random excitation in this case. In later chapter on band-limited random excitation, vibration excitation with narrower bandwidths will be investigated. A sample of time history of the applied axial pressure in one test is shown in Fig. 29 and its PSD is shown in Fig. 30. As can be observed from the figure, the input energy is concentrated within the 0-200 Hz band.

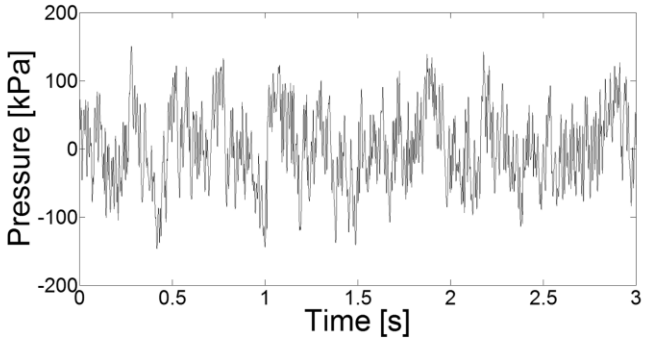

Figure 29. An example of time history of the pressure applied on stack (RMS pressure: 58 kPa).

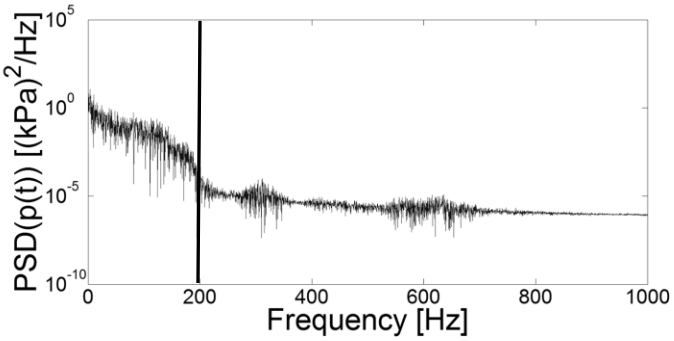

Figure 30. PSD of the pressure in Fig. 29.

When performing integration in analytical solution, PSD of pressure, $S(\omega)$, up to 200 Hz is used thus frequency limit $\bar{\omega}$ is 200 Hz. A resistor sweep from 500Ω to 20kΩ is performed. In each set of experiments, signals of force and voltage output are recorded for 3.2 seconds. For each resistive load, the test is repeated five times. From Eq. (62), the expected (mean) power is computed. The five standard deviation results at each resistive load are then averaged. In order to compare responses of the harvester, the same experimental procedure is repeated for three pressure levels: 29 kPa, 44 kPa, and 58 kPa (RMS values).

At each pressure level, the experimental measurements are plotted and compared against analytical and numerical predictions as given in Fig 31. Very good agreement is observed between the experimental results and model predictions (both analytical and numerical solutions).

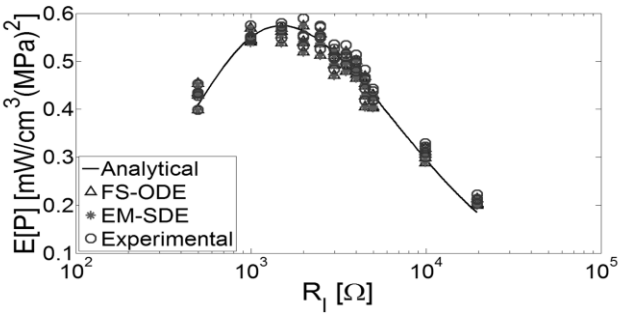

Figure 31. Comparison of experimental results, numerical simulations, and analytical predictions of power generation (normalized with respect to the stack volume and input pressure) at a pressure level 58 kPa.

Then the maximum expected power versus rms values of pressure is plotted in Fig. 32. A quadratic relation between maximum power and pressure is observed. This is due to the quadratic relation between pressure and its PSD.

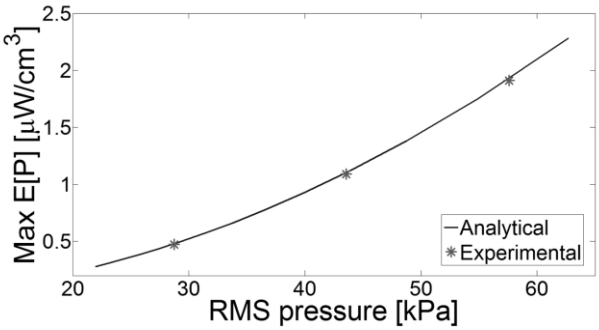

Figure 32. Experimental results and analytical predictions of maximum power generation at different pressure levels.

4.5 Comparison of various piezoelectric materials

In this section, a theoretical case study of energy harvesting from band-limited random excitation is presented for various piezoelectric materials: PZT-5H, PZT-8, PMN-PZT, PMN-PZT-Mn and PZT-5A. The piezoelectric stacks share the same geometric properties with the PZT-5H stack investigated in the previous section. The relevant material properties are given in Table 6 [44,45].

PZT-5H is a soft ceramic with larger piezoelectric coefficient (d_{33}) and larger dielectric permittivity (ε_{33}^{T}) whereas PZT-8 is a hard ceramic with smaller piezoelectric coefficient and smaller dielectric permittivity. PMN-PZT is a soft single-crystal with larger piezoelectric coefficient and larger dielectric permittivity compared to PMN-PZT-Mn, which is a hard single crystal. First, the analytical FRFs are generated, and then expected power is computed using analytical integrations in Eq. (58). The same broadband random excitation time histories in the experiments are employed in the simulations.

Table 6. Piezoelectric, and dielectric properties of the materials where $\varepsilon_0 = 8.854\text{pF/m}$ is the permittivity of free space

	PZT-5H	**PZT-8**	**PMN-PZT**	**PMN-PZT-Mn**	**PZT-5A**
d_{33} [pm/V]	650	225	1530	1140	390
d_{33}^{eff} [nm/V]	110	38.	260	193	66
$\varepsilon_{33}^{T} / \varepsilon_0$	3800	1000	4850	3410	1800
C_p [nF]	1745	459	2227	156	826

4.5.1 Electroelastic FRFs

The analytical FRFs of five different piezoelectric materials are plotted in Figs. 33-37.

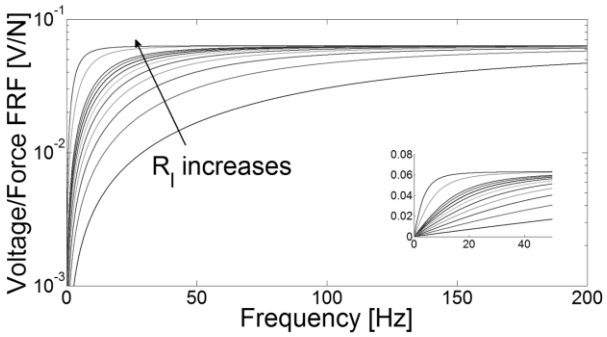

Figure 33. Voltage – to – force FRFs of the PZT-5H stack for a set of resistors.

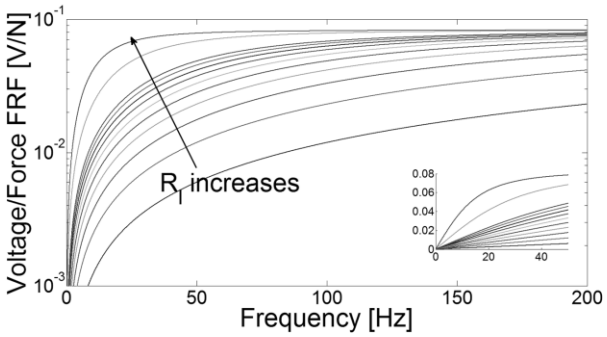

Figure 34. Voltage – to – force FRFs of the PZT-8 stack for a set of resistors.

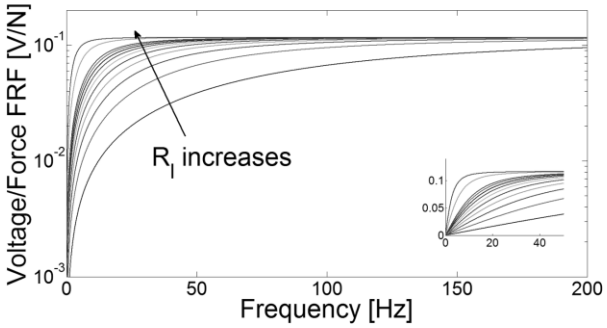

Figure 35. Voltage – to – force FRFs of the PMN-PZT stack for a set of resistors.

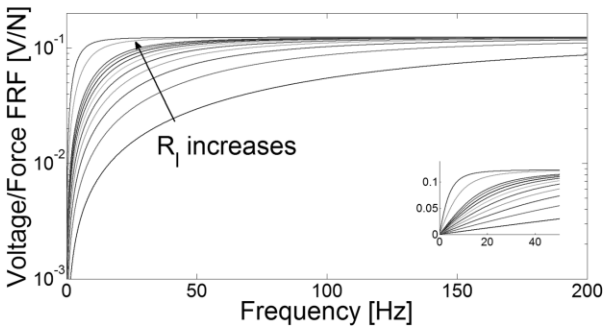

Figure 36. Voltage – to – force FRFs of the PMN-PZT-Mn stack for a set of resistors.

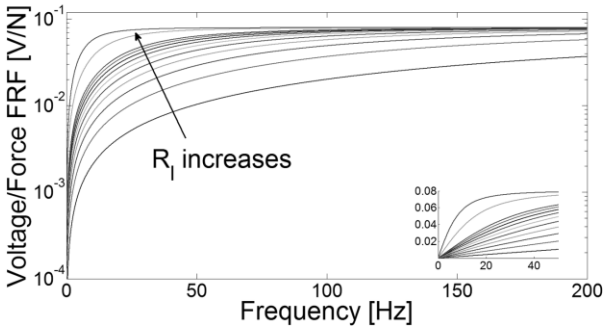

Figure 37. Voltage – to – force FRFs of the PZT-5A stack for a set of resistors.

4.5.2 Expected value of the electrical power output

Using the information of analytical FRFs and broadband random excitation from the experiments in previous sections, the expected value of the electrical power output of energy harvester using these five piezoelectric materials is computed. As shown in Fig. 38, PMN-PZT generates the largest power output from band-limited random excitation, and it is followed by PMN-PZT-Mn, PZT-5H, PZT-5A and PZT-8.

It is found that single crystals (PMN-PZT, PMN-PZT-Mn) outperform ceramics (PZT-5H, PZT-5A, PZT-8) for the same piezoelectric volume. Moreover, soft ceramics outperform

hard ceramics, while soft single crystals outperform hard single crystals. Table 7 summarizes the requirement of stack volume for generating 1 mW mean power under 1 MPa RMS pressure.

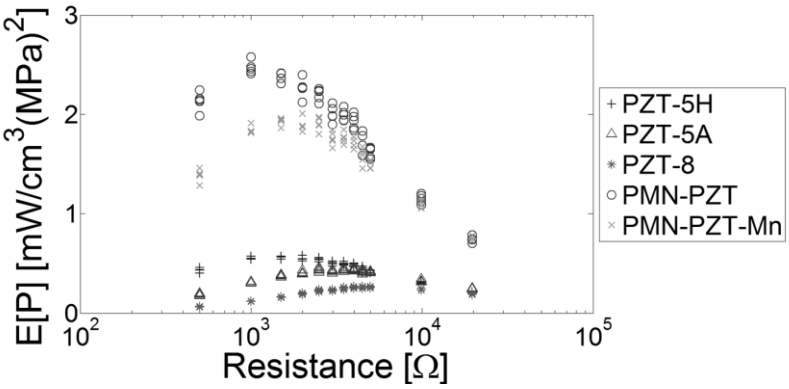

Figure 38. Expected power output (normalized with respect to the stack volume and input pressure) for stacks made of different piezoelectric materials.

Table 7. Comparison of volumetric stack requirement for different piezoelectric materials to generate 1 mW mean power output under 1 MPa (=2.5 kg / 25 mm^2) RMS pressure.

	Required material volume for 1 mW mean random power generation under 1 MPa RMS random pressure [cm^3]
PMN-PZT	0.40
PMN-PZT-Mn	0.52
PZT-5H	1.78
PZT-5A	2.27
PZT-8	3.81

4.6 Conclusions

Frequency-domain analytical solution of piezoelectric energy harvesting using a multilayer stack configuration from harmonic and broadband random vibrations is presented. In addition, time-domain numerical solutions for energy generation under random vibrations are presented. The analytical and numerical predictions exhibit very good agreement with the experimental measurements taken for a PZT-5H piezostack. The analytical solutions are further validated for different levels of random excitation. It can be concluded that the analytical and numerical solutions presented in this chapter are effective tools for predicting and optimizing the performance of piezoelectric stack harvesters under broadband random excitation. Using the experimentally validated analytical solution, stacks made of various piezoelectric materials: PMN-PZT (soft single crystal), PMN-PZT-Mn (hard single crystal), PZT-5H (soft ceramic), PZT-8 (hard ceramic), PZT-5A (soft ceramic) are compared for power generation under random excitation. It is found that single crystals outperform ceramics, moreover, soft ceramics and single crystals outperform their hard counterparts because the power generation performance under off-resonant low-frequency excitation is governed by the elastic compliance and piezoelectric constant rather than the quality factor.

CHAPTER 5

BAND-LIMITED RANDOM EXCITATION OF THE CANTILEVER AND STACK CONFIGURATIONS

5.1 Cantilevered bimorph

In this section, energy harvesting from band-limited random vibrations using cantilevered bimorph is investigated. The analytical and numerical approaches discussed in previous chapters are applied here and results are validated by experimental measurements.

The cantilever investigated in this chapter is the brass-reinforced PZT-5H bimorph as described in Section 3.5.1. Shown in Fig. 39 are the analytical and experimental voltage output – to – base acceleration FRFs and tip velocity – to – base acceleration FRFs.

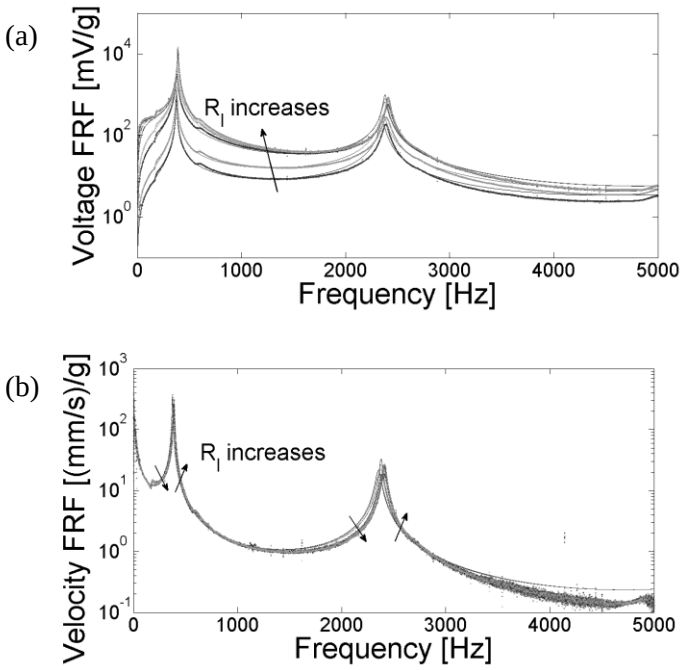

Figure 39. (a) Voltage – to – base acceleration FRFs and (b) tip velocity – to – base acceleration FRFs of the PZT-5H bimorph cantilever for a set of resistors (solid lines are analytical model and dots are experimental measurements).

In the following three sections, the bimorph is subjected to random excitations with three different bandwidths. The first set of random excitations has a frequency band from 0 to 200 Hz which does not cover any vibration mode, as can be observed from Fig 39. The second set of random excitations has a frequency band from 0 to 1 kHz, which covers the first vibration mode only. The third set of random excitations has a frequency band from 0 to 5 kHz, which covers the first and second vibration modes. The expected power generation and mean-square shunted vibration responses from the three sets of band-limited random excitations are computed using analytical and numerical solutions. The results are validated through experiments.

5.1.1 Random excitation with 0-200 Hz bandwidth

The PSD of the base acceleration is directly extracted from the data acquisition system and an example is shown in Fig. 40. As can be seen from the figure, most energy of the base acceleration is accumulated within the 0-200 Hz frequency range.

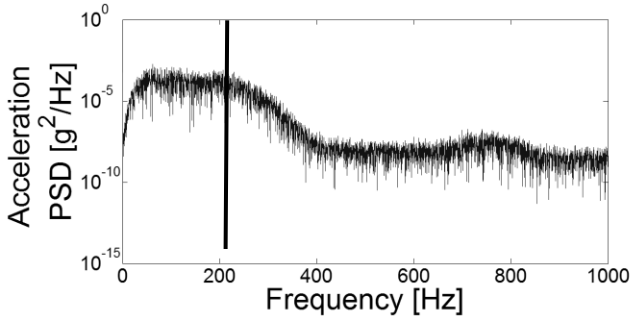

Figure 40. PSD of a 0-200 Hz random base acceleration signal.

The expected value of power output is presented in Fig. 41. Analytical prediction, two numerical solutions and experimental measurements show good agreement. The shunted vibration response (in the form of tip velocity) of the bimorph is not sensitive in this case since

the frequency band of the excitation does not cover any vibration mode. As shown in the square-mean of tip velocity vs. resistance curve (Fig. 42), no valley shape is observed.

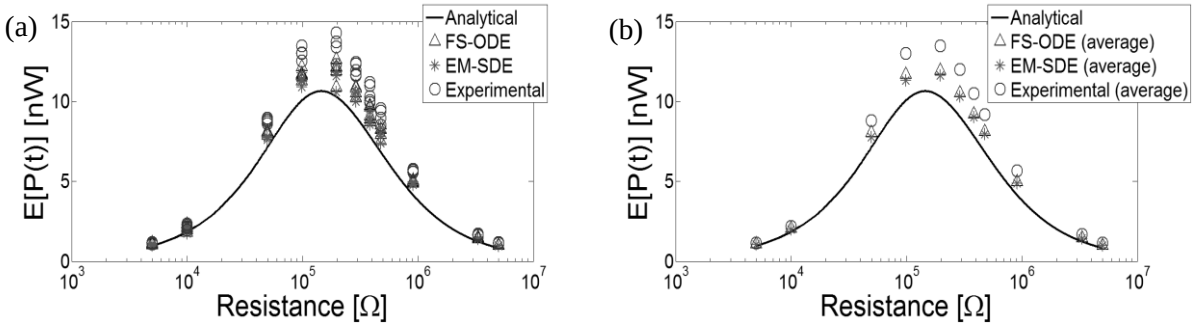

Figure 41. Comparison of analytical predictions, numerical simulations, and experimental results of expected power generation of cantilever under 0-200 Hz random excitation: (a) five experimental and numerical data points at each resistor and (b) only average values for clarity.

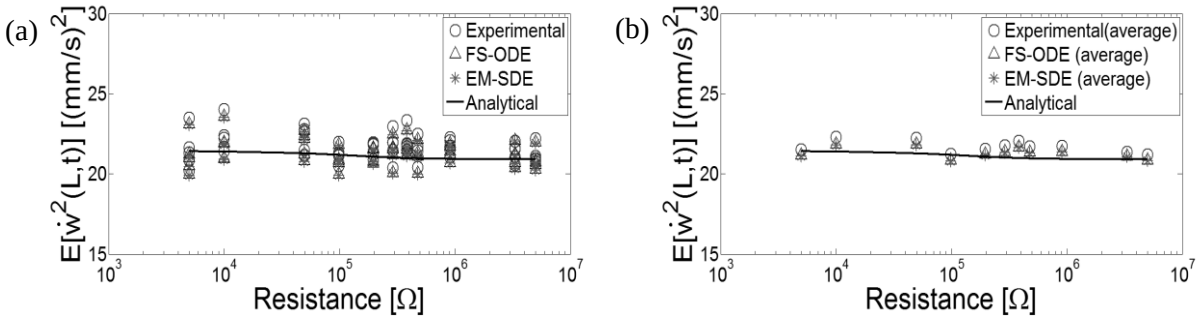

Figure 42. Comparison of analytical predictions, numerical simulations, and experimental results of mean-square tip velocity of cantilever under 0-200 Hz random excitation: (a) five experimental and numerical data points at each resistor and (b) only average values for clarity.

5.1.2 Random excitation with 0-1 kHz bandwidth

In the second case, the bandwidth of the base acceleration is from 0 to 1 kHz, its PSD is shown in Fig. 43. This excitation signal covers the first vibration mode of the system.

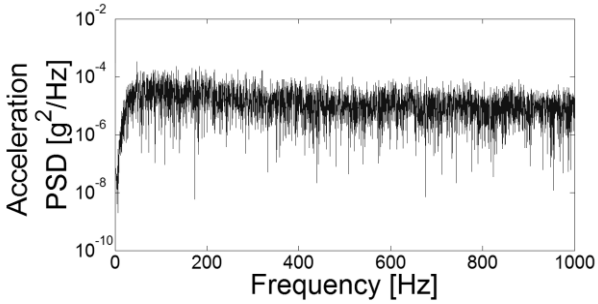

Figure 43. PSD of a 0-1 kHz random base acceleration signal.

The expected value of power output is presented in Fig. 44. Analytical prediction, two numerical solutions and experimental measurements show good agreement. Recall that this bandwidth covers the first vibration mode of the bimorph, therefore the shunted vibration response (in the form of tip velocity) of the bimorph presents a typical valley shape, as shown in Fig. 45.

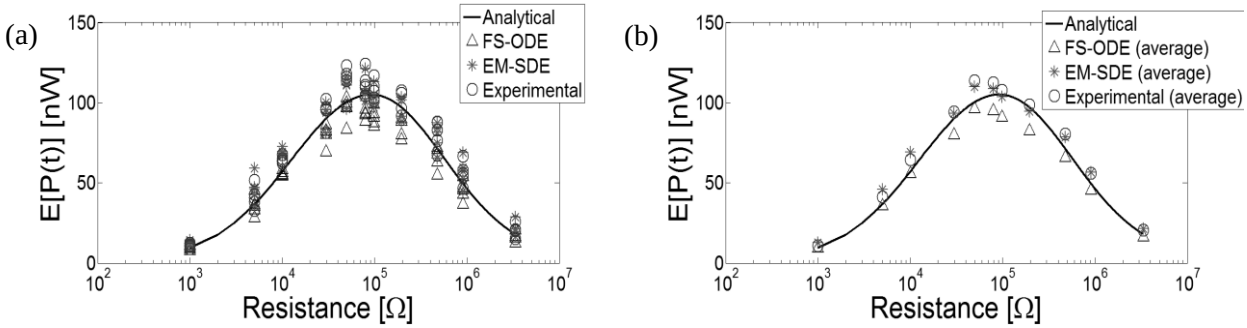

Figure 44. Comparison of analytical predictions, numerical simulations, and experimental results of expected power generation of cantilever under 0-1 kHz random excitation: (a) five experimental and numerical data points at each resistor and (b) only average values for clarity.

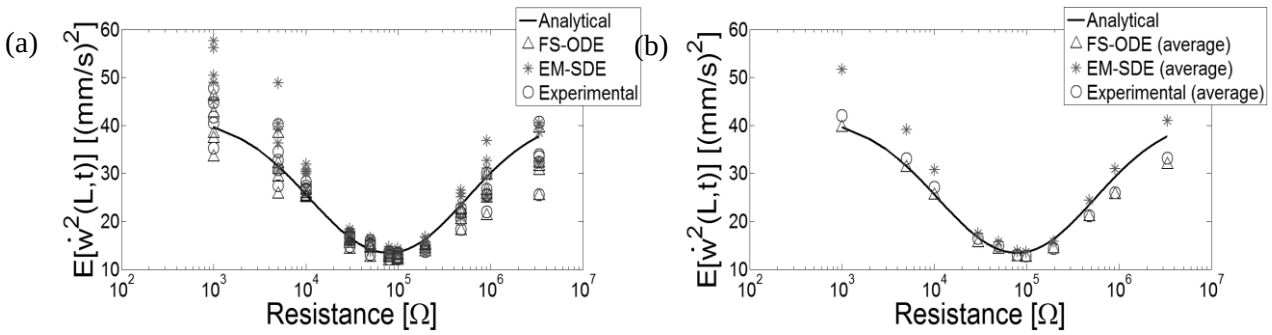

Figure 45. Comparison of analytical predictions, numerical simulations, and experimental results of mean-square tip velocity of cantilever under 0-1 kHz random excitation: (a) five experimental and numerical data points at each resistor and (b) only average values for clarity.

5.1.3 Random excitation with 0-5 kHz bandwidth

The PSD of a typical 0-5 kHz band-limited base acceleration is shown in Fig. 46.

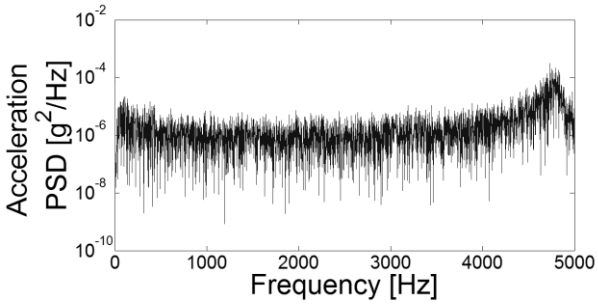

Figure 46. PSD of a 0-5 kHz random base acceleration signal.

The expected value of power output is presented in Fig. 47. Analytical prediction, two numerical solutions and experimental measurements show good agreement. The shunted vibration response (in the form of tip velocity) of the bimorph is shown in the Fig. 48. The deviations in the simulations are due to the deviations between the experimental time series.

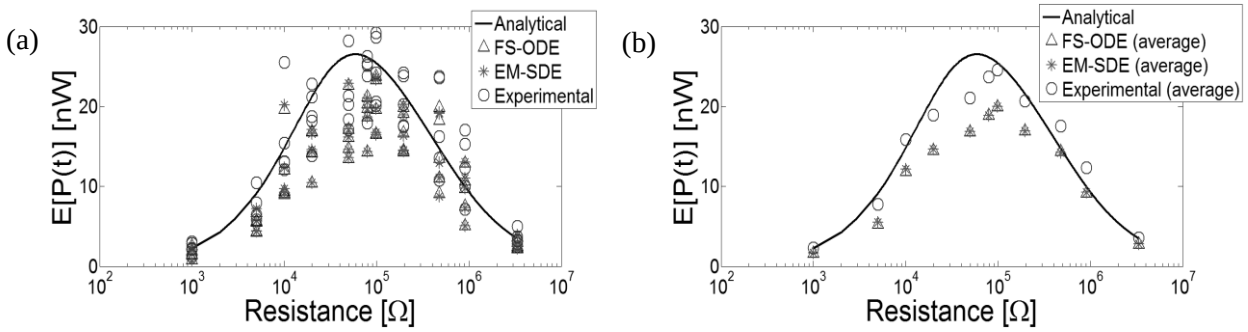

Figure 47. Comparison of analytical predictions, numerical simulations, and experimental results of expected power generation of cantilever under 0-5 kHz random excitation: (a) five experimental and numerical data points at each resistor and (b) only average values for clarity.

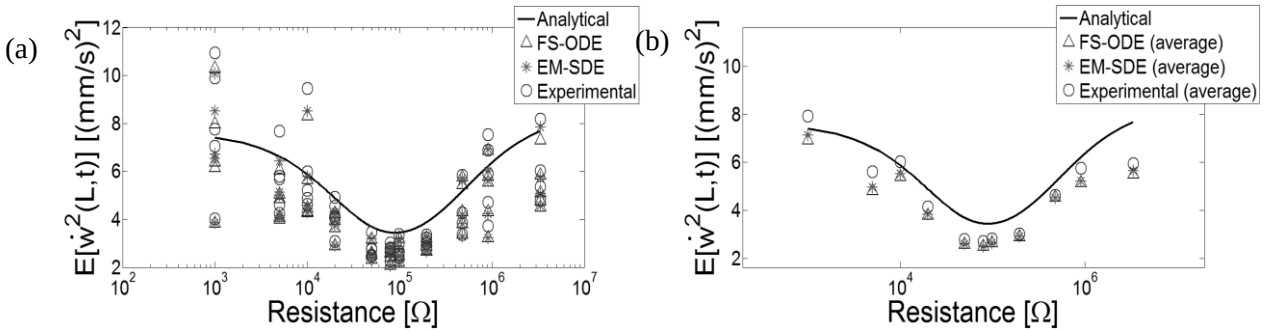

Figure 48. Comparison of analytical predictions, numerical simulations, and experimental results of mean-square of tip velocity of cantilever under 0-5kHz random excitation: (a) five experimental and numerical data points at each resistor and (b) only average values for clarity.

5.2 Multilayer piezostack

In this section, energy harvesting from band-limited random vibrations using piezostack is investigated. The analytical and numerical approaches discussed in previous chapters are applied and results are validated by experimental results. The piezostack investigated in this chapter is a PZT-5H multilayer stack as described in section 4.4.1. Shown in Fig. 49 are the analytical and experimental voltage output – to – force input FRFs.

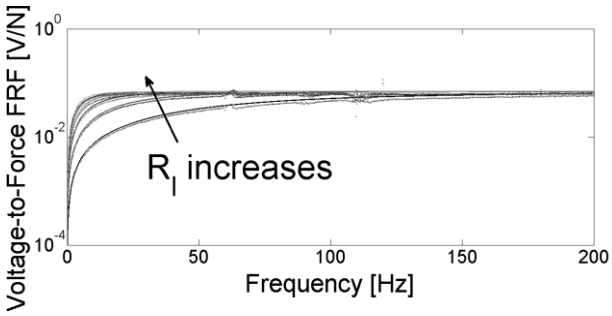

Figure 49. Voltage – to – force FRFs of the PZT-5H stack for a set of resistors (solid lines are analytical model and dots are experimental measurements).

In the following three sections, the stack is subjected to random excitation with three different bandwidths: 0-10 Hz, 0-50 Hz, and 0-140 Hz. The expected power generation and mean-square shunted vibration response from the three sets of band-limited random excitations are computed using analytical and numerical solutions. The results are validated through experiments.

5.2.1 Random excitation with 0-10 Hz bandwidth

The PSD of the axial force input is directly extracted from the data acquisition system and the PSD of a typical axial force is shown in Fig. 50. As can be seen from the figure, most energy of the axial force is accumulated within the 0-10 Hz frequency range and decays beyond about 10 Hz.

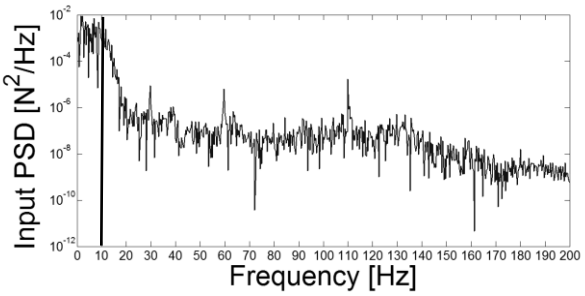

Figure 50. PSD of a 0-10 Hz random excitation signal.

The expected value of power output is presented in Fig. 51. Analytical prediction, two numerical solutions and experimental measurements show good agreement.

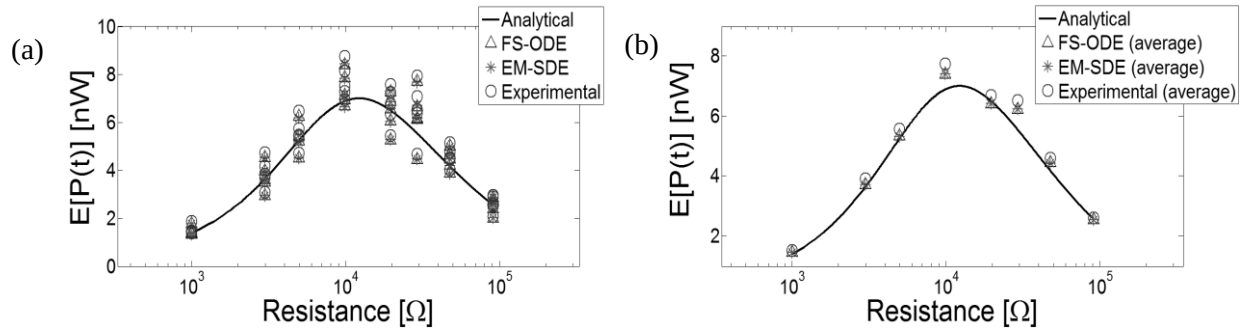

Figure 51. Comparison of analytical predictions, numerical simulations, and experimental results of expected power generation of piezostack (0-10 Hz random excitation): (a) five experimental and numerical data points at each resistor and (b) only average values for clarity.

5.2.2 Random excitation with 0-50 Hz bandwidth

The PSD of a typical 0-50 Hz band-limited axial force is shown in Fig. 52 although the decay after 50 Hz is not very sharp. As can be seen from the figure, due to the limitation of signal generator and shaker, energy of the axial force decays over the frequency band. Since energy beyond 50 Hz is negligible, it is fair to assume that the excitation has a band limit of 0-50 Hz.

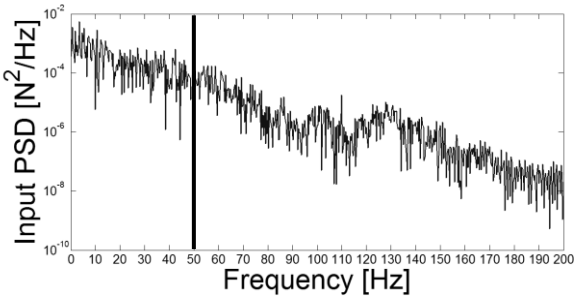

Figure 52. PSD of a 0-50 Hz random excitation signal.

The expected value of power output is presented in Fig. 53. Analytical prediction, two numerical solutions and experimental measurements show good agreement.

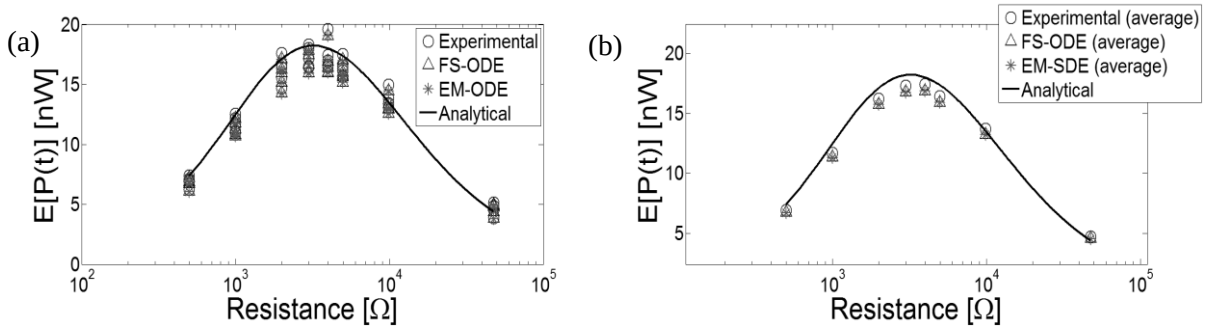

Figure 53. Comparison of analytical predictions, numerical simulations, and experimental results of expected power generation of piezostack (0-50 Hz random excitation): (a) five experimental and numerical data points at each resistor and (b) only average values for clarity.

5.2.3 Random excitation with 0-140 Hz bandwidth

The PSD of a typical 0-140Hz band-limited axial force is shown in Fig. 54. As can be seen from the figure, most energy of the axial force is accumulated within the 0-140 Hz frequency range and decays beyond about 140 Hz.

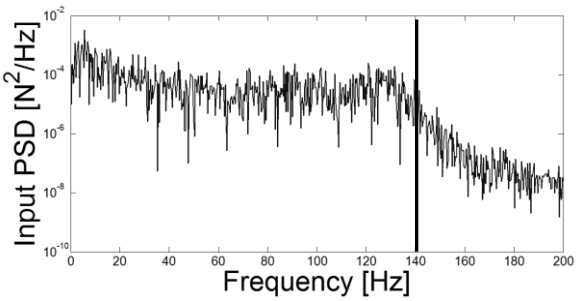

Figure 54. PSD of a 0-140 Hz random excitation signal.

The expected value of power output is presented in Fig. 55. Analytical prediction, two numerical solutions and experimental measurements show good agreement again.

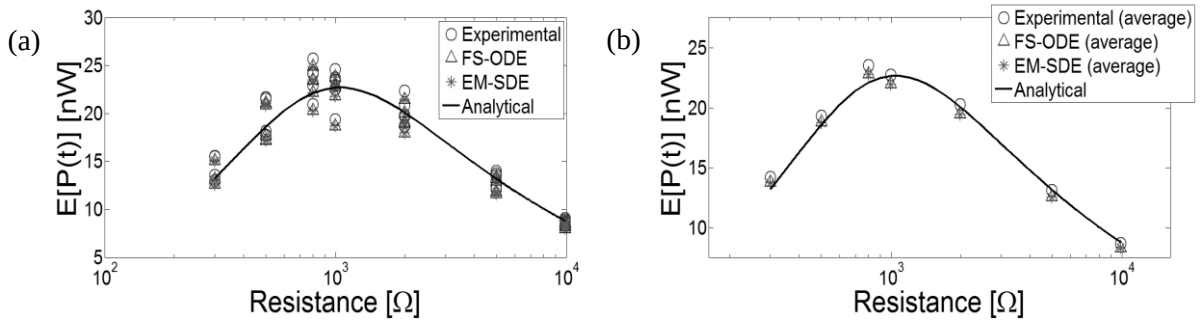

Figure 55. Comparison of analytical predictions, numerical simulations, and experimental results of expected power generation of piezostack (0-140Hz random excitation): (a) five experimental and numerical data points at each resistor and (b) only average values for clarity.

5.3 Conclusions

In this chapter, energy harvesting from band-limited random excitation of cantilever and stack configurations is investigated. Analytical and numerical solutions of the expected power output and mean-square shunted vibration response are validated through experiments using a PZT-5H cantilevered bimorph and a PZT-5H multilayer stack.

The frequency-domain analytical solution uses the PSD information of the excitation and the analytical FRFs of the harvester. In this chapter, only one time history of experimental

random excitation is used for expected power output estimation, that is, time history of excitation is fixed for varied resistance values. Since time history of excitation has variations in each experimental case, the analytical solution (one single curve) might deviate from numerical and experimental results. Numerical solutions use time history of excitation from each experimental case. Overall, the analytical and numerical results show very good agreement with experimental measurements, therefore the established mathematical tools are shown to be effective to predict the harvesters' performance and capable of handling band-limited random vibration input.

CHAPTER 6

CONCLUSIONS AND FUTURE WORK

6.1 Conclusions

This thesis presents a study of piezoelectric energy harvesting from broadband random vibrations using a cantilevered bimorph and a multilayer stack. Analytical and two numerical solutions of expected (mean) piezoelectric power output and the mean-square vibration response of each harvester configuration are developed and experimentally validated. The analytical solution uses the combination of distributed-parameter electroelastic FRFs with the input power spectral density (PSD) while the numerical solutions treat the random base excitation problem in two separate approaches deterministically and stochastically. The deterministic approach represents the base acceleration history in terms of its Fourier series expansion to use with the first-order electroelastic equations in a Runge-Kutta-based ordinary differential equation (ODE) solver while the stochastic approach directly employs an Euler-Maruyama scheme to solve the resulting first-order stochastic differential equations (SDEs). The analytical as well as ODE-based and SDE-based numerical predictions exhibit very good agreement with the experimental measurements in both studies of cantilevered bimorph and multilayer stack. The analytical and numerical solutions are further validated for different levels of random excitation. It can be concluded that the solutions presented in this thesis are effective tools for predicting and optimizing the performance of cantilevered piezoelectric harvesters and multilayer stack harvesters under broadband random excitation.

In the base-excited cantilevered bimorph case, the effect of higher vibration modes is also investigated based on the analytical solution. It is concluded that lightly damped higher vibration

modes can alter the expected power curve (primarily the optimal load) if the PSD of input vibration covers frequencies of higher modes as in the case of white noise excitation.

Using the experimentally validated analytical solution, cantilevered bimorphs made of four piezoelectric materials PZT-5H (soft ceramic), PZT-8 (hard ceramic), PMN-PZT (soft single crystal), PMN-PZT-Mn (hard single crystal) are compared for power generation under broadband random excitation. It is found that hard ceramics and single crystals outperform their soft counterparts. In addition, hard ceramics (PZT-8) can outperform soft single crystals (PMN-PZT). However, the power output levels are on the same order of magnitude unlike the case of resonant excitation under harmonic input.

Through theoretical studies, stacks made of various piezoelectric materials, PMN-PZT, PMN-PZT-Mn, PZT-5H, PZT-8, PZT-5A (soft ceramic) are compared for power generation under broadband random excitation. It is found that single crystals outperform ceramics, moreover, soft ceramics and single crystals outperform their hard counterparts because the power generation performance under off-resonant low-frequency excitation is governed by the elastic compliance and piezoelectric constant rather than the mechanical quality factor.

Finally, through multiple series of experiments, the established analytical and numerical solutions are shown to work successfully for predicting the expected electrical power and shunted vibration response for the case of band-limited random excitation as well.

6.2 Recommendations for future work

The present work investigated random excitation of geometrically, materially, and electroelastically linear piezoelectric energy harvesters. Future work might consider nonlinear energy harvesters under both broadband and band-limited random excitations for the cases of essential nonlinearities and nonlinearities introduced for performance enhancement in deterministic excitation to compare the distributed-parameter behavior (e.g. modal interactions, etc.) with the existing theories based on SDOF nonlinear modeling [24,28,32]. Modeling of random vibrational energy harvesting in the presence of nonlinear storage circuits [38,51-56] can also be of interest for future research.

REFERENCES

1. Beeby, S.P., M.J. Tudor, and N.M. White, *Energy harvesting vibration sources for microsystems applications.* Measurement Science & Technology, 2006. **17**(12): p. R175-R195.
2. Priya, S., *Advances in energy harvesting using low profile piezoelectric transducers.* Journal of Electroceramics, 2007. **19**(1): p. 167-184.
3. Anton, S.R. and H.A. Sodano, *A review of power harvesting using piezoelectric materials (2003-2006).* Smart Materials & Structures, 2007. **16**(3): p. R1-R21.
4. Cook-Chennault, K.A., N. Thambi, and A.M. Sastry, *Powering MEMS portable devices - a review of non-regenerative and regenerative power supply systems with special emphasis on piezoelectric energy harvesting systems.* Smart Materials & Structures, 2008. **17**(4).
5. Hudak, N.S. and G.G. Amatucci, *Small-scale energy harvesting through thermoelectric, vibration, and radiofrequency power conversion.* Journal of Applied Physics, 2008. **103**(10).
6. Amirtharajah, R. and A.P. Chandrakasan, *Self-powered signal processing using vibration-based power generation.* Ieee Journal of Solid-State Circuits, 1998. **33**(5): p. 687-695.
7. Roundy, S., P.K. Wright, and J. Rabaey, *A study of low level vibrations as a power source for wireless sensor nodes.* Computer Communications, 2003. **26**(11): p. 1131-1144.
8. Mitcheson, P.D., et al., *MEMS electrostatic micropower generator for low frequency operation.* Sensors and Actuators a-Physical, 2004. **115**(2-3): p. 523-529.
9. duToit, N.E., B.L. Wardle, and S.G. Kim, *Design considerations for MEMS-scale piezoelectric mechanical vibration energy harvesters.* Integrated Ferroelectrics, 2005. **71**: p. 121-160.
10. Wang, L. and F.G. Yuan, *Vibration energy harvesting by magnetostrictive material.* Smart Materials & Structures, 2008. **17**(4).
11. Erturk, A. and D.J. Inman, *An experimentally validated bimorph cantilever model for piezoelectric energy harvesting from base excitations.* Smart Materials & Structures, 2009. **18**(2).
12. Mann, B.P. and N.D. Sims, *Energy harvesting from the nonlinear oscillations of magnetic levitation.* Journal of Sound and Vibration, 2009. **319**(1-2): p. 515-530.
13. Stanton, S.C., et al., *Nonlinear piezoelectricity in electroelastic energy harvesters: Modeling and experimental identification.* Journal of Applied Physics, 2010. **108**(7).
14. Friswell, M.I. and S. Adhikari, *Sensor shape design for piezoelectric cantilever beams to harvest vibration energy.* Journal of Applied Physics, 2010. **108**(1).
15. Bai, X.L., et al., *A magnetoelectric energy harvester with the magnetic coupling to enhance the output performance.* Journal of Applied Physics, 2012. **111**(7).
16. Aureli, M., et al., *Energy harvesting from base excitation of ionic polymer metal composites in fluid environments.* Smart Materials & Structures, 2010. **19**(1).
17. Shu, Y.C. and I.C. Lien, *Analysis of power output for piezoelectric energy harvesting systems.* Smart Materials & Structures, 2006. **15**(6): p. 1499-1512.

18. Renno, J.M., M.F. Daqaq, and D.J. Inman, *On the optimal energy harvesting from a vibration source.* Journal of Sound and Vibration, 2009. **320**(1-2): p. 386-405.
19. Erturk, A. and D.J. Inman, *Parameter identification and optimization in piezoelectric energy harvesting: analytical relations, asymptotic analyses, and experimental validations.* Proceedings of the Institution of Mechanical Engineers Part I-Journal of Systems and Control Engineering, 2011. **225**(I4): p. 485-496.
20. Stanton, S.C., B.A.M. Owens, and B.P. Mann, *Harmonic balance analysis of the bistable piezoelectric inertial generator.* Journal of Sound and Vibration, 2012. **331**(15): p. 3617-3627.
21. Halvorsen, E., *Energy Harvesters Driven by Broadband Random Vibrations.* Journal of Microelectromechanical Systems, 2008. **17**(5): p. 1061-1071.
22. Adhikari, S., M.I. Friswell, and D.J. Inman, *Piezoelectric energy harvesting from broadband random vibrations.* Smart Materials & Structures, 2009. **18**(11).
23. Scruggs, J.T., *An optimal stochastic control theory for distributed energy harvesting networks.* Journal of Sound and Vibration, 2009. **320**(4-5): p. 707-725.
24. Daqaq, M.F., *Response of uni-modal duffing-type harvesters to random forced excitations.* Journal of Sound and Vibration, 2010. **329**(18): p. 3621-3631.
25. Barton, D.A.W., S.G. Burrow, and L.R. Clare, *Energy Harvesting From Vibrations With a Nonlinear Oscillator.* Journal of Vibration and Acoustics-Transactions of the Asme, 2010. **132**(2).
26. Cottone, F., H. Vocca, and L. Gammaitoni, *Nonlinear Energy Harvesting.* Physical Review Letters, 2009. **102**(8).
27. Ferrari, M., et al., *Improved Energy Harvesting from Wideband Vibrations by Nonlinear Piezoelectric Converters.* Proceedings of the Eurosensors Xxiii Conference, 2009. **1**(1): p. 1203-1206.
28. Litak, G., M.I. Friswell, and S. Adhikari, *Magnetopiezoelastic energy harvesting driven by random excitations.* Applied Physics Letters, 2010. **96**(21).
29. Erturk, A., J. Hoffmann, and D.J. Inman, *A piezomagnetoelastic structure for broadband vibration energy harvesting.* Applied Physics Letters, 2009. **94**(25).
30. McInnes, C.R., D.G. Gorman, and M.P. Cartmell, *Enhanced vibrational energy harvesting using nonlinear stochastic resonance.* Journal of Sound and Vibration, 2008. **318**(4-5): p. 655-662.
31. Ali, S.F., S. Adhikari, and M.I. Friswell, *Analysis of magnetopiezoelastic energy harvesters under random excitations: an equivalent linearization approach.* Active and Passive Smart Structures and Integrated Systems 2011, 2011. **7977**.
32. Daqaq, M.F., *Transduction of a bistable inductive generator driven by white and exponentially correlated Gaussian noise.* Journal of Sound and Vibration, 2011. **330**(11): p. 2554-2564.
33. Nguyen, D.S., et al., *Fabrication and characterization of a wideband MEMS energy harvester utilizing nonlinear springs.* Journal of Micromechanics and Microengineering, 2010. **20**(12).
34. Halvorsen, E., et al., *Simulation of electromechanical systems driven by large random vibrations.* Perspective Technologies and Methods in MEMS Design, 2007: p. 117-122.
35. Tvedt, L.G.W., L.C.J. Blystad, and E. Halvorsen, *Simulation of an Electrostatic Energy Harvester at Large Amplitude Narrow and Wide Band Vibrations.* Dtip 2008:

Symposium on Design, Test, Integration and Packaging of Mems/Moems, 2008: p. 296-301.
36. Blystad, L.C.J., E. Halvorsen, and S. Husa, *Piezoelectric MEMS Energy Harvesting Systems Driven by Harmonic and Random Vibrations.* IEEE Transactions on Ultrasonics Ferroelectrics and Frequency Control, 2010. **57**(4): p. 908-919.
37. Tvedt, L.G.W., D.S. Nguyen, and E. Halvorsen, *Nonlinear Behavior of an Electrostatic Energy Harvester Under Wide- and Narrowband Excitation.* Journal of Microelectromechanical Systems, 2010. **19**(2): p. 305-316.
38. Erturk, A. and D.J. Inman, *Piezoelectric Energy Harvesting*. 2011, Chichester: Wiley. xx, 392 p.
39. Erturk, A., *Assumed-modes modeling of piezoelectric energy harvesters: Euler-Bernoulli, Rayleigh, and Timoshenko models with axial deformations.* Computers and Structures, 2012 (doi:10.1016/j.compstruc.2012.05.010).
40. Meirovitch, L., *Fundamentals of vibrations*. 2001, Boston: McGraw-Hill. xviii, 806 p.
41. Newland, D.E., *An introduction to random vibrations and spectral analysis*. 1975, London ; New York: Longman. xxi, 285 p.
42. Kloeden, P.E. and E. Platen, *Numerical solution of stochastic differential equations*. Applications of mathematics. 1992, Berlin ; New York: Springer-Verlag. xxxv, 632 p.
43. Clough, R.W. and J. Penzien, *Dynamics of structures*. 2nd ed. 1993, New York: McGraw-Hill. xxii, 738 p.
44. *Morgan Technical Ceramics*. Available from: www.morgantechnicalceramics.com.
45. Zhang, S.J., et al., *Characterization of Mn-modified Pb(Mg(1/3)Nb(2/3))O(3)-PbZrO(3)-PbTiO(3) single crystals for high power broad bandwidth transducers.* Applied Physics Letters, 2008. **93**(12).
46. Goldfarb, M. and L.D. Jones, *On the efficiency of electric power generation with piezoelectric ceramic*. Journal of Dynamic Systems Measurement and Control-Transactions of the Asme, 1999. 121(3): p. 566-571.
47. Feenstra, J., J. Granstrom, and H. Sodano, *Energy harvesting through a backpack employing a mechanically amplified piezoelectric stack.* Mechanical Systems and Signal Processing, 2008. 22(3): p. 721-734.
48. Li, X.T., M.S. Guo, and S.X. Dong, *A Flex-Compressive-Mode Piezoelectric Transducer for Mechanical Vibration/Strain Energy Harvesting*. IEEE Transactions on Ultrasonics Ferroelectrics and Frequency Control, 2011. 58(4): p. 698-703. 28.
49. Erturk, A., *Piezoelectric energy harvesting for civil infrastructure system applications: Moving loads and surface strain fluctuations*. Journal of Intelligent Material Systems and Structures, 2011. 22(17): p. 1959-1973.
50. NIST TIP Internal Report by the Physical Acoustics Corporation for a 3-span steel continuous curved multi-girder bridge in Roanoke, VA.
51. Ottman, G.K., Hofmann, H.F., Bhatt, A.C., and Lesieutre, G.A.(2002) Adaptive piezoelectric energy harvesting circuit for wireless remote power supply. *IEEE Transactions on Power Electronics*, **17**, 669-676.
52. Ottman, G.K., Hofmann, H.,F., and Lesieutre, G.A.(2003) Optimized piezoelectric energy harvesting circuit using step-down converter in discontinuous conduction mode. *IEEE Transactions on Power Electronics*, **18**, 696-703.
53. Badel, A., Benayad, A., Lefeuvre, E., Leburn, L., Richard, C., and Guyomar, D. (2006) Single crystals and nonlinear process for outstanding vibration-powered electrical

generators. *IEEE Transactions of Ultrasonics, Ferroelectrics, and Frequency Control*, **53**, 673-684.

54. Badel, A., Guyomar, D., Lefeuvre, E., and Richard, C. (2005) Efficiency enhancement of a piezoelectric energy harvesting device in pulsed operation by synchronous charge inversion, *Journal of Intelligent Material Systems and Structures*, **16**, 889-901.

55. Badel, A., Guyomar, D., Lefeuvre, E., and Richard, C. (2006) Piezoelectric energy harvesting using a synchronous switch technique. *Journal of Intelligent Material Systems and Structures*, **17**, 831-839